Targeted PLGA Nanoparticles for the Sustained Release of Hypertensive Drugs

Targeted PLGA Nanoparticles for the Sustained Release of Hypertensive Drugs

Grace Giordano Ingalls

A Thesis in the Field of Bioengineering and Nanotechnology

for the Degree of Master of Liberal Arts in Extension Studies

Harvard University

March 2019

Abstract

The major objective of this project was to design and characterize a novel antibody conjugated poly(lactic-co-glycolic acid) (PLGA)nanoparticle that could successfully target human endothelial cells and provide a sustained release of hypertensive drugs, which could ultimately help to improve patient adherence by reducing the frequency of patient medication. Poor patient adherence remains one of the leading causes of inadequately controlled blood pressure in adults diagnosed with hypertension. Due to the short half-lives of most hypertensive drugs, patients are required to take multiple doses a day to keep their blood pressure under control, which decreases the likelihood of a patient's adherence. To establish proof of concept, PLGA nanoparticles were prepared with antihypertensive drugs captopril (CAP) and valsartan (VAL) using the common nanoprecipitation fabrication technique, and then modified with polyethylene glycol (PEG) molecules and ICAM-1 antibodies. Dynamic light scattering (DLS) and scanning electron microscopy (SEM) techniques were employed to characterize the size, shape, and zeta potential of the final nanoparticles, while Fourier transform infrared (FTIR) spectroscopy was used to confirm the successful conjugation of the PEG molecules. The drug loading and release characteristics of the nanoparticles are observed using a UV-Vis spectrometer. The attachment of the antibody is initially validated using a Pierce 660 nm Protein assay, and the ability of the antibody to target the pulmonary endothelium was confirmed with static and flow experiments on human umbilical endothelial vein cells (HUVECS). The results of this study indicated an

average size of 150 nm and <-10 mV zeta potential value for the final drug loaded nanoparticles, confirming the adequate size and zeta potential necessary for drug delivery. The results from UV-VIS indicated the successful encapsulation of both drugs and demonstrated a sustained release of over 100 hours for each drug. The antibody conjugated nanoparticles showed significant specificity towards the target cell type, as well as successfully adherence to the target cells under both static and flow conditions. The combination of these results indicates this formulated nanoparticle could successfully provide sustained drug delivery to a targeted area of the body, which could help to decrease the number of doses for hypertensive treatment, and subsequently increase patient adherence.

Dedication

This thesis work is dedicated to my parents, Catherine and Mark Ingalls, whose love and support have brought me to where I am today. This work is also dedicated to Christopher Micheli, who was there to always remind me of what I'm capable of and to never give up on myself.

Acknowledgments

Over the course of this thesis I have received support and encouragement from a great number of individuals. First and foremost, I'd like to thank my thesis advisor Dr. Anas Chalah, who first inspired my passion for nanotechnology, and proceeded to teach, guide, and encourage me through my entire master's degree. I'd like to thank Harvard's Active Learning Labs for providing the space to conduct my research, and to the many people who work there who've assisted me with the equipment and lab supplies.

I'd like to thank Harvard's Center for Nanoscale Systems (CNS) and the Harvard Center for Biological Imaging (HBCI) for the use of their facilities during the creation and characterization of my nanoparticles and the imaging of my cellular experiments. I'd like to thank the many staff members at both CNS and HCBI for training me on the various pieces of equipment and assisting me on optimizing the techniques required for each of these machines. The assistance of the Mitragotri lab at Harvard and the Langer lab at MIT helped to provide keen insights during the analysis of my experiments.

I am truly grateful for the help of all these people and facilities, as this thesis would not be here without them.

Table of Contents

List of Tables

List of Figures

Chapter I.

Introduction

In the United States, about 1 in every 3 adults (approximately 86 million people) have been diagnosed with hypertension (Nwankwo, Yoon, Burt, & Gu, 2013) Most treatments for hypertension require multiple administrations of the medication throughout the day, due to the extremely short half lives of the drugs. (Flesch, Muller & Lloyd, 1997). The use of nanoparticles as a platform for drug delivery has been used for the treatment of multiple types of diseases (Srivastava et al., 2016). The goal of this study is design and characterize a targeted PLGA nanoparticle for sustained release of hypertensive drugs.

Hypertension and Patient Compliance

More commonly known as high blood pressure, hypertension is defined as having a systolic blood pressure (SBP) >140 mmHg or a diastolic blood pressure (DBP) >90 mmHg (Crim et al., 2012). Having uncontrolled hypertension can put a person at risk for stroke and heart disease, which are the leading causes of death in the United States (Benjamin et al., 2017). In fact, hypertension contributes to the death of more than 410,000 Americans per year (Centers for Disease Control and Prevention, 2015). Living with chronic hypertension can cause damage to one's organs and lead to complications such as aneurysms, eye damage, or kidney disease (Mayo Staff Clinic, 2016). Despite the

risk of mortality and disease, more than 50% of people diagnosed with hypertension do not have their blood pressure under control (Alexander, 2017). Poor treatment compliance embodies a significant obstacle in control of hypertension.

Patient compliance, or treatment compliance, is defined as "the extent to which the actual time history of dosing corresponds to the prescribed regimen" (World Health Organization, 2003). Compliance is a widely underestimated problem, as physicians often expect their patients to always adhere to a prescribed treatment schedule. However, within the first two years of receiving hypertension medication, roughly 40% of patients will discontinue their treatment, up to 75% are non-adherent to the treatment, and almost 10% of patients forget to take their medication every day (Manolis, Poulimenos, & Kallistratos, 2015). Some of the factors leading to poor treatment adherence can be patient-related, such as lack of understanding of their disease and medication, or physician-related, such as failure to explain the patient's medical regime effectively (Brown & Bussels, 2011). According to the World Health Organization, this lack of adherence is the primary cause of uncontrolled BP (World Health Organization, 2003). For patients with hypertension, poor compliance can significantly increase one's risk for myocardial infarction, stroke, and hospitalization (Brown & Bussells, 2011). As anticipated, increased adherence to antihypertensive therapy significantly decreases the risk of these events. This fact is excellently demonstrated in a study by Mazzaglia et al. (2009), where it was found that patients who had 80% or higher adherence rate were at a 38% decreased risk of cardiovascular events compared to patients with lower adherence. Aside from the obvious health benefits of high patient adherence, according to the

National Pharmaceutical Council (NPC, 1992), noncompliance can cost the US up to $8.5 billion extra due to physicians' visits and hospital admissions.

There are a multitude of factors that contribute to poor treatment adherence, but one significant obstacle is the use of polypharmacy treatments. There have been multiple studies that demonstrate how patient adherence improves with fewer number of doses. *Figure 1* compares treatment adherence to number of doses per day, showing patient compliance dropping 10-15% with each additional required daily dose. For patients with hypertension, a study by Detry et al. (1995) demonstrated that not only did patients who received once daily anti-hypertensive medication have better patient compliance, but also had significantly better therapeutic coverage than patients who received twice daily medication. With the knowledge that high patient adherence decreases cardiovascular risks in hypertensive patients, and that decreases in dosing regimens increases patient compliance, it seems one logical way to increase the overall health of hypertensive patients would be to decrease the number of doses require for treatment.

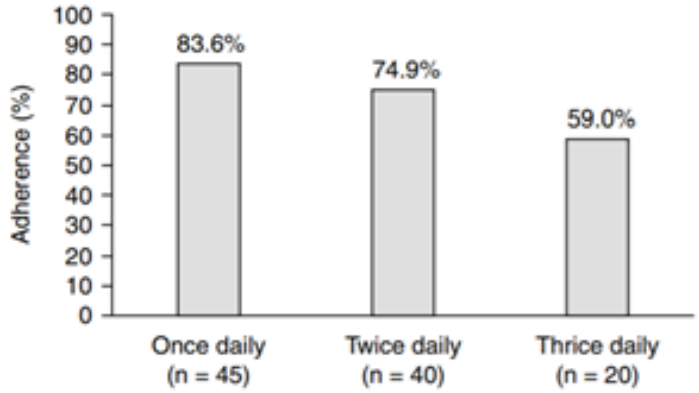

Figure 1. Mean medication adherence according to administration frequency. .

Diagram of the changes in medication adherence based on the required frequency of administration. From "Drug Delivery Systems for Treatment of Systemic Hypertension" by L.M. Prisant & W.J. Elliott, 2003, Clinical Pharmacokinetics, 42(11), 931-940.

Current Treatments & The RAAS Pathway

There are a variety of treatments available to help patients manage hypertension. An indispensable part of any treatment regimen is lifestyle modifications; weight loss, increased consumption of fruits and vegetables, regular aerobic physical activity, stopping smoking habits, and limiting alcohol intake have all been shown to help reduce BP and prevent incidences of hypertension (Chobanian, Bakris, & Black, 2003). However, for many patients with severe or late stage hypertension, lifestyle modifications are not enough to control their blood pressure. In fact, over two-thirds of individuals will require two or more antihypertensive agents from different drug classes to successfully control their hypertension (Turnbull, 2003).

There are a variety of different classes of oral antihypertensive drugs, including thiazide diuretics, aldosterone receptor blockers, beta blockers, angiotensin-converting enzyme inhibitors (ACEIs), angiotensin II receptor blockers (ARBs), vasodilators, and calcium channel blockers (Chobanian, Bakris, & Black, 2003). Each of these classes of drugs help to reduce blood pressure by targeting a different area of the body. One pathway commonly targeted for hypertension is the renin-angiotensin-aldosterone system (RAAS). *Figure 2* features a diagram detailing the different components involved in the RAAS pathway.

The RAAS pathway is activated when the body senses a decrease in blood pressure or fluid volume, which stimulates the biosynthesis of renin from the renin precursor prorenin, which is released from the kidneys. Renin is secreted into blood circulation, where it will interact with a large molecular weight globulin secreted from the liver; angiotensinogen. Renin will cleave the N-terminal portion of angiotensinogen,

forming the decapeptide angiotensin I (Ang I). This molecule remains inactive until it encounters the exopeptidase angiotensin-converting enzyme (ACE), which removes the C-terminal dipeptide to form the octapeptide angiotensin II (Ang II). This molecule is the primary active product of the RAAS pathway, and it works to increase blood pressure in several ways. Ang II interacts directly with receptors on the surface of blood vessels to stimulate vasoconstriction, as well as interacting with the adrenal cortex to increase the production and release of aldosterone. The hormone aldosterone acts on organs such as the kidney and colon to enhance the reabsorption of salt and water into the bloodstream, which increases blood volume and therefore blood pressure (Cagnoni et al., 2010; Manrique, Lastra, Gardner & Sowers 2009; Weir & Dzau, 1999).

The drug classes ACEIs and ARBs are used to target the RAAS pathway and help decrease blood pressure, and the drugs Captopril and Valsartan were chosen from these classes to use in this experiment. Captopril, an ACEI, works by binding to ACE molecules and preventing the enzyme from converting Ang I to Ang II (National Center for Biotechnology Information, 2005). This reduces the amount of Ang II in the blood stream, which reduces its vasoconstriction effects (Turnbull, 2003). The other drug, Valsartan, is an ARB which targets the RAAS pathway downstream after Ang I has already been converted into Ang II (National Center for Biotechnology Information, 2005b). These drugs work by competitively binding to the Ang II receptors on blood vessel walls, blocking the molecule from interacting with the receptor, and eliminating the vasoconstriction effects (Izzo & Weir, 2011).

Although there are many types of drugs used in the treatment of hypertension, this study uses the ACEI Captopril and the ARB Valsartan for several reasons. The most

common medication prescribed for hypertension (in terms of prescriptions written) are ACEIs (Morelli & Ogbru, 2016). However, over 65% of patients require more than one type of hypertension medication for the most effective treatment (Chobanian, Bakris, & Black, 2003). The combination of an ACEI with an ARB has been shown to significantly decrease BP compared to individual drug treatment (Azizi et al., 2000, Stergiou et al., 2000). One of the reasons a combination of ACEIs and ARBs is more effective than monotherapy treatment is because other enzymes aside from ACE can form Ang II. It is vital to have both an upstream drug target (ACEIs) and a downstream target (ARBs) to address the RAAS pathway when treating hypertension.

Although both Captopril and Valsartan have been shown highly effective in reducing BP, one of the biggest limitations of these medicines is their extremely short half-lives, 2 hours and 4 hours respectively (Duchin, Singhvi, Willard, Migdalof & Mckinstry, 1982, Flesch, Muller & Lloyd, 1997). Because these drugs have such short half-lives, patients are required to administer doses multiple times a day to keep the drugs consistently active. The nanoparticle developed in this study can help to increase the half-life time of these drugs by providing a sustained release of medication over a longer period. As shown in the sections above, patients who take fewer doses a day have a much higher rate of compliance and are at a reduced risk of the dangerous cardiovascular complications associated with uncontrolled BP. If one were able to reduce the number of doses required for the drugs Captopril and Valsartan, it would be possible to increase patient compliance and thus improve patients BP and overall health.

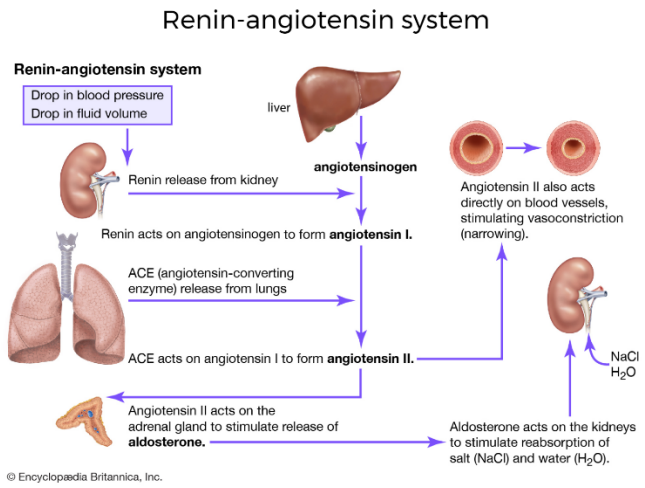

Figure 2. Diagram of the Renin-Angiotensin System.

The Renin-Angiotensin System, also known as the renin-angiotensin aldosterone system (RAAS), is one of the pathways in the body that controls blood pressure. From "The Editors of Encyclopaedia Britannica (Ed.). (n.d.). Renin-angiotensin system. In Encyclopaedia Britannica. Encyclopaedia Britannica."

PLGA Nanoparticles

The use of poly(lactic-co-glycolic acid) nanoparticles (PLGA NPs) could help to reduce the dosing frequencies of Captopril and Valsartan, as well as enhance the drugs' bioavailability. PLGA, poly-(glycolic acid) (PGA), and poly-(lactic acid) (PLA) were first discovered in the 1960s and used for surgical sutures (Cutright, Beasley & Perez, 1971). Since then there has been increasingly growing interest in using these materials as polymeric biomaterials, with PLGA now being considered the most well known and widely used biodegradable polymer for drug delivery (Srivastava et al., 2016).

The structure of PLGA consist of a polyester backbone formed from the copolymerization of the monomers lactic and glycolic acid (Hines & Kaplan, 2013). The composition of PLGA is the reason it has many of the unique properties useful for drug

delivery. The monomers lactic and glycolic acid are endogenous and metabolized easily by the body, giving the polymer minimal toxicity to organs and tissues (Kumari, Yadav & Yadav, 2010). Due to PLGAs high level of biocompatibility, it is approved for humans in multiple drug delivery systems by both the European Medicine Agency (EMA) and the US FDA (Alam et al., 2017, Danhier et al., 2012). Because PLGA is a copolymer, it can be polymerized with different compositions of lactic and glycolic acid monomers, which will change the properties of the polymer; for example, due to the higher hydrophobicity of lactic acid, using a high lactic acid to glycolic acid ratio would result in a more hydrophobic PLGA. This change is useful when loading a hydrophobic drug into the NP, as the heightened hydrophobicity of the device will result in a more uniform drug dispersion through the matrix (Hines & Kaplan, 2013, Jain, 2000). Because of the composition versatility of PLGA, these NPs can carry a large variety of cargo, including small hydrophilic and hydrophobic drugs, vaccines, proteins, and biological macromolecules (Sharma, Parmar, Kori & Sandhir, 2016).

Another advantage of being able to control the copolymer ratio is that the composition of the PLGA can help control the degradation rate of the NP (Uhrich, Cannizzaro, Langer & Shakesheff, 1999, Jain, 2000). The degradation of PLGA occurs through the hydrolysis of the copolymers polyester backbone (Houchin & Topp, 2008). This process happens when water penetrates the PLGA matrix, activating the process of polymer degradation. As the degradation process proceeds, lactic and glycolic acid monomers erode away from the device, which in turn allows for the diffusion of the encapsulated drugs away from the NP. This process can be influenced by several properties, but the copolymer ratio heavily contributes to the rate of degradation; water

permeation can be slowed by designing the PLGA with a higher hydrophobic monomer ratio (Hines & Kaplan, 2013, Uhrich, Cannizzaro, Langer & Shakesheff, 1999).

The use of PLGA NPs in drug delivery not only offers the ability to carry numerous types of cargo and control the degradation rate of the polymer, but it also allows for modification of the NPs' surface. The ability to modify the NPs surface offers several advantages, the first being evasion of the body's immune system. Opsonin proteins present in the blood stream attach themselves to hydrophobic particles, which signals macrophages to internalize and eliminate the foreign object (Danhier et al., 2012). The foreign body response to injected NPs is a major hurdle in targeted polymer drug delivery (Sah, Thoma, Desu, Sah & Wood, 2013). In 1994, Gref et al. was able to address this problem by modifying the surface of a PLGA NP with the hydrophilic, non-ionic polymer, polyethylene glycol (PEG). This modification resulted in 45% increase in circulating NPs when compared to uncoated NPs. Not only can surface modification of NPs help to avoid recognition from the body's immune system, but it can be used to help target specific tissues or organs in the body. Modifying a NPs surface with a cell-targeting ligand ensures the NP will bind to a specific receptor, where the drug can then be released and reach its target more efficiently (Murciano et al., 2003). For targeted drug delivery systems, a smaller amount of drug can be used to achieve the same therapeutic effect seen in free dose drugs, which are more likely to be cleared by the immune system before reaching their target (Singh & Lillard, 2009).

With PLGA NPs known effects against degradation, enhanced sustained release, and increased circulation ability, its application has greatly expanded in multiple fields of medicine, including hypertension. Since many drugs used in the treatment of

hypertension have low bioavailability or are quickly metabolized by the bodies system, the use of PLGA NPs has helped to increase these drugs efficiency. The use of small anti-hypertensive peptides encapsulated in PLGA NPs was studied by Yu et al. (2016) to analysis the devices in vivo antihypertensive effect. Peptides Ile-Pro-Pro (IPP) and Val-Pro-Pro (VPP), peptides known for their antihypertensive effect, are loaded into PLGA NPs and administered to spontaneously hypertensive rats. These PLGA and drug combinations, labelled VP5-NPs, showed a remarkably decrease in systolic blood pressure compared to control groups and free VP5 drug groups. Another study done by Jana et al. (2014) tested the in vitro release profile of felodipine loaded PLGA NPs. Felodipine, a CCB largely used for systemic arterial hypertension treatment, when loaded into PLGA NPs, exhibited at least 96 hours of slow drug release, which is a markedly significant increase when compared to the less than 20-hour drug release of the marketed formulation of felodipine. These studies are excellent examples of how versatile and effective PLGA NPs can be in the treatment of hypertension.

In 2015, Arora et al. explored the idea of drug delivery with PLGA NPs even further by combining multiple drugs together for the sustained release of hypertensive drugs. The authors of this study chose three different classes of hypertensive drugs for their NP fixed dose combination (NanoFDC); amlodipine besylate (a CCB), candesartan (an ARB), and hydrochlorothiazide (a diuretic). The NanoFDC device offers an additional advantage over the previously discussed works, as it's been shown that the combination of different classes of hypertensive drugs results in an additional decrease in blood pressure when compared to single drug therapy (Azizi et al., 2000). The in vitro release study showed a 100% drug release rate of 4 days for amlodipine and candesartan,

and up to 15 days for hydrochlorothiazide. The authors were able to replicate these results in vivo by testing the plasma levels of drug administered spontaneous hypertensive rats. The NanoFDC group had all three drugs present in plasma levels up to 6 days after administration, which is a significant increase from free dose drug groups where the drugs were only found up to 24 hours after administration. As the authors stated in the discussion, "Our study has shown for the first-time sustained levels lasting for nearly 7 days of the 'NanoFDC' containing commonly co-prescribed drugs for hypertensive patients." This type of device could significantly help address the problem of poor adherence and therapeutic failure.

While the NanoFDC demonstrates a huge advancement in sustained release technology and a possible solution to the problem of poor patient compliance, it has no type of surface modification that could potentially improve the devices efficiency. Due to the intrinsic negative charge of bare PLGA NPs, unmodified NPs are rapidly removed from blood circulation, which would impact the duration of drug release (Sah, Thoma, Desu, Sah & Wood, 2013). The addition of PEG molecules could help to circumvent that problem. Not only is the NanoFDC not concealed as it circles the blood stream, but it also has no cell recognition or tissue target. For drugs that target the RAAS system, such as ACEIs and ARBs, the primary targets are ACEs, and the ACEs' product, Ang II. Although some ACE molecules can be found in blood circulation, the majority of the enzymes involved in the RAAS pathway are located on the surface of pulmonary endothelial cells (Orfanos et al., 1999). This would be an ideal target for PLGA NPs that deliver ACE drugs. The antibody inter-cellular adhesion molecule-1 (ICAM-1) has been shown effective at binding to pulmonary vascular cells for the delivery of antithrombotic

drugs, and can easily be linked to PLGA NPs for targeted drug delivery (Murciano et al., 2003). With the addition of PEG stealth modification and ICAM-1 targeting, the PLGA NP will be a highly effective system for delivering RAAS targeted antihypertensive drugs.

ICAM-1 Antibody

Numerous studies over the last decade have demonstrated the improved therapeutic efficiency of targeted drug delivery compared to non-targeted methods (Muzykantov, 2013; Muro & Muzykantov, 2005). The intercellular adhesion molecule 1 (ICAM-1) receptor has been a popular target for the diagnostic and therapeutic treatment of a variety of diseases. ICAM-1's are type 1 transmembrane glycoproteins composed of three sections; an intracellular section to interact with the cells cytoskeleton, a section that traverses the cell membrane, and an extracellular section which is responsible for interactions with other cells and chemicals (Mohaimen, Sami, Al-assady & Ali, 2013, Rothlein & Wegner, 1992).

ICAM-1 plays a significant role in endothelial signaling and T-cell activation; the overexpression of ICAM-1 receptors promotes leukocyte adhesion and activation, which in turn signals for cytoskeleton remodeling allowing the leukocytes to migrate through the endothelial layer (Bélizaire, Tchistiakova & Alakhov, 2003, Blair, Haven & Bauer, 2016). ICAM-1 proteins are present in several cell types, but the surface density of ICAM-1 receptors is particularly high in vascular endothelial cells (Muzykantov, 2013). Since more than 25% of endothelial cells are located in the pulmonary vasculature, compounds with ICAM-1's antibody, known as anti-ICAM-1, are known to accumulate in the lungs (Ferrer et al., 2014). The ICAM-1 molecules located on the endothelial

luminal surface are ready accessible to the circulation, which makes it an ideal target for drug delivery to the pulmonary endothelium (Muro et al., 2006).

Given the accessibility and localization of ICAM-1, it has already been used as a target for the treatment and diagnosis of a variety of diseases. In a previous study of ICAM-1, Chittasupho et al. (2009) developed an ICAM-1 targeted NP for the delivery of the anti-cancer drug doxorubicin to carcinomic lung epithelial cells. They found that compared to bare NP, the ICAM-1 targeted NPs had a significantly higher binding and uptake into the cells in vitro. Since many chemotherapeutics can be highly toxic to healthy cells, having a targeted delivery system would greatly reduce the nonspecific dosing of healthy tissues.

In the body, the major site of thrombosis in many cases is the pulmonary vasculature. Monoclonal ICAM-1 antibodies have been used for targeting and delivering antithrombotic drugs to the pulmonary vascular lumen. Murciano et al. (2003) published a comprehensive study of anti-ICAM directed drug delivery in a variety of conditions, including in vitro cell cultures, perfused lungs, and in vivo animals. They were able to show specific targeting to the endothelium in all conditions, as well as demonstrating anti-ICAM's ability to target the surface with and without cellular internalization. The ability to control cellular internalization is extremely useful, as many drugs that are only active once internalized have no native way of entering the target cell.

Not only is the pulmonary endothelium an important target for thrombosis, but it is a major site of inflammation in cases such as acute lung injury or respiratory distress (Howard et al., 2014). Ferrer et al. (2014) aims to address the issue of inflammation with a novel anti-ICAM conjugated nanogel for the delivery of the inflammatory inhibitor

dexamethasone (DEX). This study showed successful accumulation of the ICAM-nanogel in mouse lungs, as well as effective release of DEX to block upregulation pro-inflammatory cell adhesion. Because ICAM-1 is upregulated at sites of inflammation, it becomes not only a target for drug delivery, but also an advancement in anti-inflammation treatment, as the binding of the nanogel to ICAM-1 receptors prevents inflammation molecules from adhering to the cell.

Although there are a variety of blood stream targets used for drug delivery, ICAM-1 offers specific advantages for this study. One significant advantage of targeting ICAM-1 is that receptor expression is upregulated in the pulmonary artery endothelium of hypertensive patients (Blair, Haven & Bauer, 2016). This is to be expected, as it's been proven that extensive hypertension can lead to damaged blood vessels, and ICAM-1 is upregulated in damaged/inflamed endothelium (Mayo Staff Clinic, 2016). This upregulation results in ICAM-1 accumulation in the lungs, which is where the primary source of one of the drugs target molecules (ACE) is produced and surface bound (Howard et al., 2014, Orfanos et al., 1999). Not only is ICAM-1 an extremely relevant target for hypertension, but it's been shown in multiple experiments that anti-ICAM ligands can be easily conjugated to the surface of NPs, giving us the ability to transport anti-hypertensive drugs to a highly specific and relevant target site (Zhang et al., 2008, Gonzolez-Rodriguez & Barakat, 2015).

As stated earlier, the pulmonary vasculature holds the majority of the body's membrane bound ACE molecules, which is the target molecule for hypertensive drugs. Using ICAM-1 to target the pulmonary endothelium directs our NP towards these target molecules. For this method to provide consistent targeting, it's important that the NP

remains bound to the targeted surface while it releases the hypertensive drugs. Previous studies have shown that anti-ICAM carriers are able to withstand shear stress over 3 times the amount seen in blood vessels without detaching from the cells (Calderon, Muzykantov, Muro & Eckmann, 2009, Bhowmick et al., 2012). The firm adhesion of anti-ICAM conjugates to the surface of pulmonary vasculature provides PLGA NPs the opportunity to deliver the sustained release of hypertensive drugs to a targeted area.

Chapter II.

Materials and Methods

The following section describes the materials and techniques used in this study. The nanoparticles used in the study are first be and characterized to confirm its various properties. Briefly, PEG molecules are attached to the PLGA to create a PEG-PLGA copolymer. Cargo loaded PEG-PLGA nanoparticles (PEG-PLGA NPs) are produced via the nanoprecipitation method, and then functionalized with anti-ICAM-1 molecules for cellular targeting. After the final ICAM conjugated PEG-PLGA NPs (ICAM NPs) are formed, they are characterized to understand their physical and chemical properties. After the characteristics of the NPs are confirmed, the binding capabilities are tested under both static and flow conditions.

PEG-PLGA Synthesis

Before the PLGA NP's can be formed, the first step is to synthesize the deblock co polymer PEG-PLGA. The conjugation of these two polymers is achieved using an EDC/NHS chemical reaction. In this reaction EDC will couple the NHS molecule to the the carboxylic acid end of the PLGA, forming an NHS ester end group. This amine reactive NHS ester can easily be displaced by a primary amine (PEG-NH2), which will then form an amide bond with the original carboxyl group, giving us our final PEG-PLGA copolymer (Zhang et al., 2008, Gonzolez-Rodriguez & Barakat, 2015). This process starts by dissolving 100 mg of PLGA [acid terminated, lactide:glycolide 50:50,

Mw 24,00-38,000] (Milipore Sigma, St. Louis, MO) , 100 mg EDC [1-ethyl-3-(3-dimethylaminopropyl) carbodiimide hydrochloride] (Thermo Scientific, Rockford, IL) , and 60 mg NHS [N-Hydroxysuccinimide] into 5 ml of chloroform in solvent hood. The top is covered to limit solvent evaporation, and the solution is mixed on a magnetic stir plate at room temperature for 2 hours. One the EDC/NHS reaction has finished, 20 ml of methanol is added to precipitate the activated PLGA-NHS. This solution is centrifuged with an Avanti J-26 XP centrifuged (Beckman Coulter, Brea, CA) for 30 minutes, at 18,000 RPM and at 4°C. The supernatant is discarded, and the PLGA-NHS pellet is redissolved in 5 ml of chloroform, and 33 mg of NH2-PEG-COOH [carboxyl-amino poly(ethylene glycol), MW: 3.5K] (Advanced BioChemicals, Lawrenceville, GA) is added to the solvent. This solution is capped and stirred overnight, allowing the PEG-NH2 to conjugate to the PLGA-NHS. Once the final PLGA-PEG copolymer is formed, it is precipitated with 20 ml of methanol, and can be collected by centrifuging the solution at 18,000 RPM, for 30 mins at 4°C.

Nanoparticle Formation vis Nanoprecipitation

Once the PLGA-PEG copolymer has been formed, it can be used to create drug loaded PLGA-PEG NPs. These NPs are created through a method called nanoprecipitation (aka solvent displacement). This technique, one of the first techniques for fabricating drug encapsulating nanoparticles, involves the dropwise addition of a polymer organic solution into an aqueous medium for the formation of NPs. To create the organic phase, the polymer (PLGA-PEG) and the hydrophobic cargo are dissolved into a

water miscible solvent. This phase is then slowly added drop by drop into a rapidly stirring aqueous solution, containing de-ionized water and a surfactant to stabilize the final emulsion. As the organic phase meets the aqueous solution, the solvent will rapidly diffuse away resulting in the precipitation of the polymer at the water/organic interface. This polymer deposition leads to the spontaneous formation of the colloidal suspension of drug encapsulated NPs. This process starts by dissolving 100 mg PEG-PLGA in 12 ml of acetone, and place in Branson 2510 Ultra sonic cleaner (Marshall Scientific, Hampton NH) until dissolved (about 10 minutes) to form the organic solution. The organic solution is divided in two, and either 12 mg of Captopril (Milipore Sigma, St. Louis, MO) or 12 mg of Valsartan (Milipore Sigma, St. Louis, MO), (Thermo Scientific, Rockford, IL) is added to the organic solution. The organic phase is slowly added to a 50 ml of stirring 2.5% poly(vinyl alcohol) [PVA. Mw 13,000-23,000](Milipore Sigma, St. Louis, MO) aqueous solution using an NE-4000 2 channel syringe pump (New era Pump Systems Inc., Farmingdale NE) at 20 ml/hr. The emulsion is stirred (600 RPM) for 4 hours to allow solvent to fully evaporate, then centrifuged at 18,000 RPM (4C) for 30 mins to collect the NPs

ICAM-1 Antibody & Alexa 488 Attachment

The fully formed PLGA-PEG NPs can be further modified by attaching an anti-ICAM-1 antibody to the surface of the NPs to allow for targeted drug delivery. This antibody conjugation can be achieved using the same EDC/NHS chemical reaction used to attach the PEG molecules to the PLGA polymer. 50 mg of PLGA-PEG NP pellets are

resuspended in 2.5 ml of ph6 MES buffer (Milipore Sigma, St. Louis, MO), with the addition of 15 mg of NHS (50 mM) and 50 mg of EDC (100 mM), and incubated at room temperature for 1 hour with gentle stirring. The activated PLGA-PEG NPs are collected by centrifuging for 30 minutes, 18,000 RPM, at 4C, and washed with 1X phosphate-buffered saline [PBS] (Thermo Scientific, Rockford, IL) to remove residual EDC/NHS. The activated PLGA-PEG NPs are resuspended in 2.5 ml of PBS, and different molecules added to create various NP groups. For ICAM-NPs, 50 ul of anti-human CD54 [ICAM-1] antibody (BioXCell, West Lebanon, NH) is added; for Alexa-NPs, 20 ul of Alexa Fluor 488 NHS Ester (Thermo Scientific, Rockford, IL) is added; for Alexa-ICAM-NPs, both ICAM and Alexa amounts are added. For all three types of NP additions, the solution is stirred at room temp overnight to allow for antibody or fluorescent attachment. The NP's are then collected by centrifuging for 30 mins, 18,000 RPM, at 4C, and washed 2 times with PBS. These finalized NPs can then be characterized to understand their physical and chemical properties.

Size and Zeta Potential Analysis

Dynamic light scattering (DLS) techniques can be used to characterize the size and zeta potential of the NPs. 5 mg NPs are suspended in 5 ml diH20 and loaded into a disposable cuvette. Size measurements are measured with a DelsaNano C particle size analyzer (Beckman Coulter, Brea CA). Size, intensity, and volume distributions are calculated, as well as the polydispersion index (PDI). Data is accumulated 70 times, and

repeated twice to gain accurate results. Zeta potential is measured using a Zetasizer (Malvern Instruments, Malvern UK).

Size Confirmation and Morphology Analysis

To confirm the size and morphology of the NPs, measurements are taken with a field emission scanning electron microscope (FESEM). Nanoparticles are suspended in di ionized water, and ~10ul dropped onto carbon tape, allowed to dry overnight. After drying, carbon tape is placed onto SEM specimen stub, and prepped for SEM using a 150T S Metal Sputter Coater (Quorum, Lewes UK). Samples are coated with an 80/20 platinum palladium blend to a thickness of 5 nm. After samples are sputter coated, they are imaged with an Supra55VP FESEM (Carl Zeiss, Oberkochen, Germany). After images are obtained, the size of the individual particles is measured using ImageJ software.

PEG Attachment Analysis

To confirm the attachment of the PEG molecule to the PLGA, fourier transform infar red (FTIR) spectroscopy is used. Desiccated samples of unmodified PLGA, unmodified PEG, and the PLGA-PEG formation are read using a Nicolet iS50 FTIR Spectrometer (Thermo Scientific, Rockford, IL). Spectrums are collected at wavelengths 400-4000 (cm^{-1}) for each of the samples, and these absorbance spectrums and then compared to analyze PEG attachment.

ICAM-1 Antibody Attachment Analysis

Attachment of the ICAM-1 antibody to the surface of the PEG-PLGA nanoparticle can be confirmed using a Pierce 660 nm Protein Assay (Thermo Scientific, Rockford, IL). Standards are created by diluting bovine serum albumen (BSA) in PBS at concentrations from 0-250 ug/ml. ICAM-1 conjugated PEG-PLGA nanoparticles, and unconjugated PEG-PLGA nanoparticles are dispersed in 1X PBS. In a clear polystyrene 96 well plates, add 10 ul of each replicate of standard samples and ICAM-1 conjugated NP samples into separate wells. All samples are done in triplicate. 150 ul of Protein Assay Reagent is added to each well, the plate is covered with tinfoil and mixed on a plate shaker at medium speed for 1 minute, then incubated at room temperature for 5 minutes. The absorbance of the standards and the unknown samples are measured at 660 nm.

Alexa Attachment Analysis

Attachment of the fluorescent molecule Alexa 488 to the surface of the PEG-PLGA nanoparticle is confirmed using a SpectraMax M2 Microplate Reader (Molecular Devices, San Jose CA). Both Alexa conjugated NPs and blank NPs are dispersed in diH20, and 150ul of each sample is loaded into separate wells of 96-well solid black polystyrene microplate (Corning Inc., Corning NY). Samples are excited with 488 nm laser, and fluorescence of each of the samples is measured at 520 max emission and compared for analysis. The amount of Alexa 488 attachment can be measured using the

linear regression equation derived from an Alexa 488 standard curve. For these measurements, different concentrations of Alexa 488 (100 ng/ml to 400 ng/ml) are diluted in cell media, and 3 samples of 150 ul of each concentration are added to a black polystyrene micro plate and measured at the same excitation/emission as indicated above. For this analysis, Alexa 488 is dispersed in cell media instead of water, as this is the medium the Alexa-NPs will be dispersed in during flow binding experiments. To ensure the level of fluorescent is accurate, the same medium is used for the Alexa 488 calibration curve. To determine how much Alexa 488 is attached to the NPs, Alexa conjugated NPs are lyophilized and weighed, and dissolved in cell medium to create different concentrations of Alexa NP media (15 ug/ml to 250 ug/ml). Three samples of each concentrations are analyzed using the microplate reader, and the amount of Alexa per milligram of NP can be calculated using the linear regression curve generated from the Alexa 488 standard concentration plot.

Drug Loading and Release Studies

Once the final drug encapsulated NPs are formed, they drug loading and release abilities of the NPs can be tested. These experiments start by resuspending the freshly formed NPs in diH20 at a concentration of 1 mg/ml and placed in to RLS Tubular clear glass serum vials (Med Lab Supply, Pompano Beach FL) The vials are frozen at -70 C for four hours, then moved to a Freezone 2.5 vacuum dryer (Labconco Corp., Kansas City MO) set at a condenser temperature of -45 C and vacuum dried at 0.2 mBar using a

rotary vane vacuum pump (Labconco Corp., Kansas City MO) for 24 hours. After initial drying, the pressure is lowered to 0.06 mBar for another 24-48 hours until the NPs are completely dry. These lyophilized NPs are weighed and the weight is recorded for drug loading and release experiments.

To test the drug loading and encapsulation efficiency, 5 mg of lyophilized NPs are dissolved in 1 ml of acetonitrile and sonicated for 5 mins in a sonicator to aid in complete dissolution of the PLGA NPs. The PLGA is precipitated by adding 5 ml of methanol, then the solution is centrifuged for 30 mins at 18,000 RPM to pellet the PLGA particles. The supernatant containing the previously encapsulated drug is analyzed by placing 2.5 ml of the solution in 10 mm standard rectangular quartz cuvette (Vernier Sotwar, Beaverton OR) and measured with a Cary 60 UV-Vis Spectrometer (Agilent Technologies, Santa Clara CA). The absorbance is recorded at specific wavelengths (205 nm for Valsartan, and 210 nm for Captopril), and these measurements are compared to a calibration curve created with different concentrations of Captopril and Valsartan dissolved in the same ratio of acetonitrile and methanol to obtain the concentration of drug in the solution. Once the concentration of the encapsulated drug has been obtained, these values are used to measure the drug loading and encapsulation efficiency of each drug using the following equations:

$$Drug\ Loading\ \% = \left(\frac{weight\ of\ drug\ in\ NP}{weight\ of\ NP}\right) * 100$$

$$Encapsulation\ Efficeincy\ \% = \left(\frac{weight\ of\ total\ drug\ added - weight\ of\ drug\ in\ NP}{weight\ of\ total\ drug\ added}\right) * 100$$

To understand the rate of drug release from the NPs, 5 mg lyophilized ICAM conjugated drug encapsulated NPs are weighed and dissolved in 2 ml of Phosphate Buffered Saline (PBS) 10X (MediaTech Inc, Manassas VA) at a ph 7.4. This study specifically uses ICAM-NPs for release experiments as opposed to unconjugated drug encapsulated NPs, to ensure the conjugation of the antibody to the surface of the NP does not effect the release of the drug. The NP solution is sonicated for 5 mins to aid in NP dispersion, and then the NP suspension is loaded into prepared 10K MWCO Slid-A-Lyzer Dialysis Cassette (Themo Scientific, Rockford IL). These cassettes are submerged in 100 ml of PBS (sink medium) and the entire container placed in a Max Q 4000 shaking incubator (Thermo Scientific, Rockford IL) at 150 RPM and 37C to simulate the physiological conditions that would be expected in the body. The top of the containers are covered with tinfoil to avoid liquid evaporation, and at various time points 5 ml of the sink medium are withdrawn and replaced with fresh PBS. The sink medium is immediately analyzed using a UV-Vis spectrometer, and the absorbance is recorded and compared to a calibration curve of various concentrations of the drug dissolved in 10X PBS. These absorbance values can now be converted to drug concentrations, and the release rate of the drug is measured until the drug concentration in the sink medium does not change (indicating the total amount of drug has been released from the NPs).

Static Cell Experiments

The receptor activation and NP binding studies are preformed using Human Umbilical Endothelial Cells [HUVECs] (Thermo Scientific, Rockford IL) between passage 4 and 7. The cell medium used in this experiment is a combination of 98 ml of M200 medium (Cascade Biologics, Grand Island NY), 2 ml of 50X low serum growth supplement (Cascade Biologics, Grand Island NY), and 20 ul of gentamycin solution (50 mg/ml) (VWR Life Science, Sanborn NY). To aid in cell attachment, the surfaces of the culture plates are coated in 5 ug/ml of human fibronectin (Corning Inc., Corning NY), incubated at 37 C for 2 hours to allow for adherence of the fibronectin, and then washed three times with 1X Hanks Buffered Saline Solution [HBSS] (Gibco, Grand Island NY) to remove excess fibronectin. Cells are seeded at confluency (0.2×10^6 cells/well) into a 24 well culture plate (Corning Inc., Corning NY), and incubated overnight at 37 C with 5% CO2 to allow for cell attachment. After the cells have adhered to the plate, they are activated with 5 ng/ml of Human TNF α (Shenandoah, Warwick PA). The cells are treated with TNF α for 24 hours to increase ICAM receptor density to mimic the physiological conditions of hypertensive patients. After TNF α activation, the cells are washed twice with PBS, and are ready for nanoparticle experiments.

TNF α Activation and ICAM Receptor Density Confirmation

TNF α is used to increase the ICAM receptor density on the surface of the cell body. To test the amount of ICAM receptor density, various concentrations of TNF α are

incubated with the HUVECs for 24 hours, then the cells are fixed with 4% paraformaldehyde (PFA) (Electron Microscopy Sciences, Hatfield PA) for 10 mins to crosslink the cells and prepare them for fluorescent staining. The PFA is removed and the cells are washed twice to remove any excess chemical, then 5 ug/ml of the ICAM primary antibody is added and allowed to incubate overnight at 4C. After incubation, the cells are washed twice with PBS to remove excess antibody, then 4.92 ng/ml of Hoechst 3342 (Thermo Scientific, Rockford IL) and 1:500 dilution of Alexa 488 donkey anti-mouse IgG secondary antibody (Thermo Scientific, Rockford IL) added and incubated at room temperature for 2 hours to allow for nuclear staining and secondary antibody attachment. The cells are washed twice, and then imaged using a Cell Discoverer fluorescent microscope (Carl Zeiss, Oberkochen Germany). The amount of anti-ICAM antibody fluorescence is quantified using ImageJ software, and then compared to select the ideal TNF α concentration for NP binding experiments.

Nanoparticle Static Cell Binding Experiments

The selectivity and total amount of NP binding under static conditions can be tested using 24 hour TNF activated HUVEC cells. The TNF α media is removed and the cells are washed with warmed PBS, which is then removed and replaced with the appropriate concentration of NP media. To choose the best concentration of NP's, a range of NP concentrations is incubated for 2 hours at 37C to allow for attachment, and then removed and replaced with fresh PBS. After the cells are washed with PBS to remove any unbound NPs, they are fixed in the same procedure as described above. The PFA is

removed, the cells are washed twice with PBS, then incubated with fluorescent stains. The cells are stained with a 1:2500 dilution of Hoechst to visualize the nucleus (10 mins at room temperature), a 1:500 dilution of Alexa Fluor 499 phalloidin (Thermo Scientific, Rockford IL) to visualize the cell body (12 hours at 4C), and a 1:500 dilution of Alexa 568 donkey anti-mouse IgG antibody (Thermo Scientific, Rockford IL) to visualize the ICAM conjugated nanoparticles. For experiments conducted with non ICAM conjugated NPs, the phalloidin stain is omitted so there is no interference with the NP fluorescence. The amount of NP binding can be quantified by measuring the level of fluorescence using ImageJ software. The NP concentration that shows the most amount of binding with the least amount of cellular death is chosen for continuing NP binding experiments

Once the ideal concentration of NPs has been determined, several important properties of the NPs can be tested; the timeline of NP binding, the importance of the ICAM antibody in NP binding, and the ability to bind to TNF α activated or non-activated HUVEC cells. To determine the amount of time it takes for NP's to bind, 250 ug/ml of ICAM-NPs are incubated with TNF α activated HUVECs for different lengths of time, and then washed and fixed for imaging. The amount of NP binding is quantified using the same methods described above, providing information on how quickly the ICAM NP's can bind to activated HUVECs. In parallel with the ICAM-NP binding timeline, un conjugated Alexa-NPs are also tested to demonstrate the necessity of the ICAM antibody for NP binding. To demonstrate this trait, 250 ug/ml of unconjugated Alexa-NPs are incubated with TNF α activated HUVECs for the same periods of time and imaged to determine amount of NP binding. The impact of the ICAM antibody on NP binding can be determined by comparing the level of fluorescence between the

ICAM-NPs and the unconjugated Alexa-NPs. To ensure that the NPs do not bind to cells that don't display the ICAM receptor, 250 ug/ml of ICAM-NP and unconjugated Alexa NPs are incubated for 4 hours with either TNF α activated HUVECs or untreated (non-activated) HUVECs. The level of NP fluorescence is compared between the NP treated TNF α activated and non-activated cells to confirm the selective binding of the NPs

Flow Chamber Construction and Assembly

After demonstrating the ability for NPs to bind under static conditions, its essential to confirm their ability to bind to cells under shear stress. There are several commercially available systems designed to apply fluid stress to cell cultures, however these pieces of equipment are not readily available in most laboratories, and the purchase of these machines are a minimum of $40,000 (Conant, Schwartz, Nevil, 2009). Due to the budget constraints of this project making the purchase of this equipment unfeasible, a flow chamber was designed and built to test shear stress instead. The flow chamber fabricated for this thesis was constructed based on a previously defined protocol (Lane et al., 2012). This system is designed to allow for a defined fluid shear stress, real-time observation of cell morphology, easy collection of perfusate, and recovery of cells after the experiment.

The design of the flow chamber consists of two pieces of 6061 Aluminum Alloy (McMaster-Carr, Elmhurst IL) which have been cut and machined to allow for fluid inflow and outflow, as well as slots for cell coated microscope slides and a viewing chamber. Figures 3 and 4 show the dimensions for the machining of the top plate, which

consists of the inlet and outlet, the fluid reservoirs, and the viewing chamber. Figure 5 lists the dimensions for the features on the bottom plate, which holds the slot for the cell seeded microscope slide. The final machined products can be viewed in Figure 6. Once the two plates are screwed together, they create an internal chamber with a width of 1.748 cm and a height of 0.0305 cm. These fixed dimensions allow for the calculation of the flow rate needed to reach the desired shear stress level (15 dynes/cm^2). The following equation is used to calculate flow rate:

$$Q = \frac{\tau \cdot w \cdot h^2}{6 \cdot u}$$

where $\boldsymbol{Q}$ is the desired flow rate, $\boldsymbol{\tau}$ is the target shear stress acting tangentially on the cells, $\boldsymbol{w}$ is the width of the flow chamber, $\boldsymbol{h}$ is the height of the flow chamber, and $\boldsymbol{u}$ is the viscocity of the flow medium. The viscosity is recorded at0.009 g cm^{-1} s^{-1}), as this is a typical viscosity found in cell medium (Paz et al., 2012). Given all of the known variables for the equation, the flow rate required for adequate shear stress in this flow chamber is calculated at 27 ml/min. To create fluid movement through our chamber, cell media is perfused through a series of L/S Masterflex 16 tubing (Masterflex, Gelsenkirchen, Germany) connected to the flow chamber inlet and outlets, converging to a media reservoir bottle. The set up for the completed flow circuit and flow chamber can be seen in Figure 7E. The flow movement is controlled using a cartridge pump model # 72-320-128 (Thermo Scientific, Rockford, IL), which is designed to display flow output as rotations per minute (RPM). To determine what RPM corresponds to the desired flow rate, a calibration curve can be run testing the amount of fluid moving through the pump's tubing at different RPM's for 60 seconds. Once the correct RPM is identified, the

set up is ready to be used for flow binding experiments.

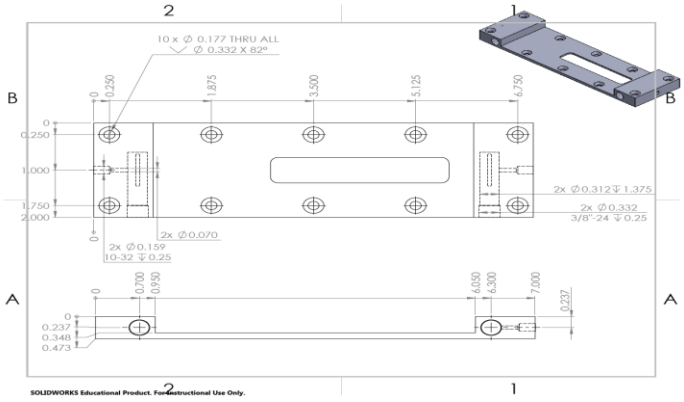

Figure 3. Solidworks Drawing of Top Plate: Top View

The computer animated drawing of the flow chamber top plate, listing the dimensions of the various components that require machining. View is from the top and side of the plate.

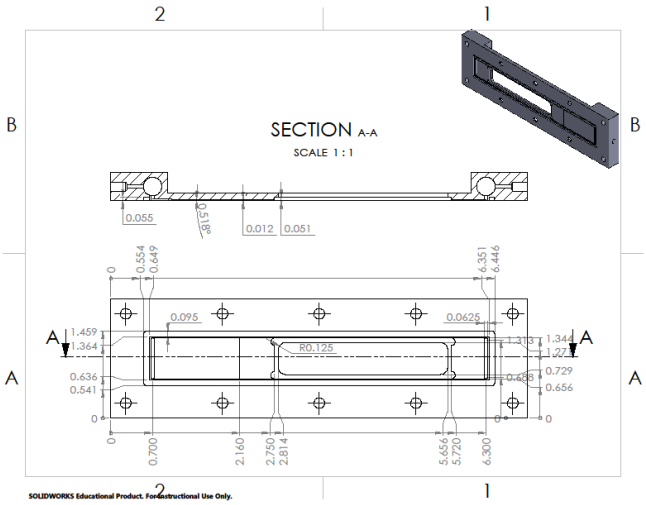

Figure 4. Solidworks Drawing of Top Plate: Side and Bottom View.

The computer animated drawing of the flow chamber top plate, listing the dimensions of the various components that require machining. View is from the bottom and side of the plate.

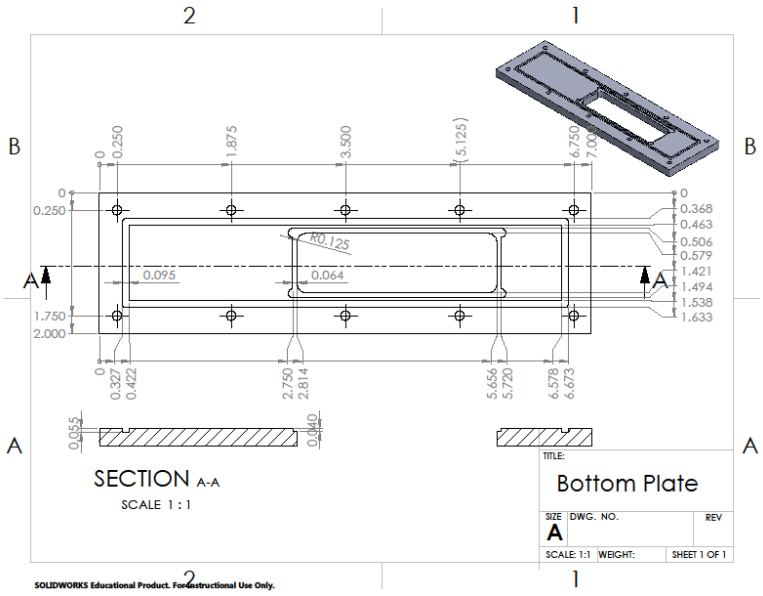

Figure 5. Solidworks Drawing of Bottom Plate.

The computer animated drawing of the flow chamber bottom plate, listing the dimensions of the various components that require machining. View is from the to, and a cross section from the side.

Figure 6. Photo of the final Machined Flow Chamber.

Image of the final flow chamber product after all completed machining. The top plate (located in the bottom of the photo) and the bottom plate (located in the top of the photo).

Nanoparticle Flow Binding Exp

The ICAM-NPs ability to bind to activated HUVECs are tested in static conditions, which provides preliminary information on the binding ability of the nanoparticles. However, the introduction of shear stress during NP binding could seriously affect the binding ability of the NP. Since these NPs are designed to bind to the lung pulmonary vasculature, the ability of the NPs to bind under flow is essential if targeted delivery of the drug is needed. To test the NP binding capacity under physiologically relevant flow, HUVECs are seeded on 25 x 75 x 1 mm micro slides (VWR Life Sciences, Sanborn NY), which are then placed into the flow chamber and adapted to flow conditions for 24 hours. The flow adapted HUVECs are then perfused with ICAM-Alexa-NP media, and various tests are conducted to test for NP binding. It has been shown that cells have a low binding affinity for glass surfaces and prefer to attach to plastic, making plastic wells and plates the preference when growing cells (Grabowski & Mcdonnell, 1993). However, to ensure the ability to visualize the cells under a microscope, the use of glass slides is essential for these experiments. For this reason, microscope glass slides are coated using the same fibronectin protocols as listed above, which were previously used with no toxicity to the cells. Once the glass slides have been coated in fibronectin and washed thoroughly, HUVECS are seeded at confluency (1.5×10^6 cells) onto the surface of the slide and are incubated overnight to allow for adequate cell adhesion. The cells are then washed twice with PBS, and fixed and stained using the same protocols implemented for static binding experiments. To visualize the cells under the microscope, they must first be mounted and dried for

imaging. To prepare the slides for imaging, the slides are removed from the final PBS wash and excess PBS is gently removed from the surface of the slide to allow for solid attachment of the coverslip. Two 22 x 40 mm micro coverglass slips (Electron Microscopy Sciences, Hatfield PA) are cleaned with 70% ethanol to remove debris and allowed to air dry before use. The cell coated microscope slide is prepared by added a small drop (<10 ul) of prolong gold antifade reagent (Invitrogen, Eugene OR) to the slide surface, then the ethanol cleaned coverslips are carefully placed onto the mounting media, and gently pressed down to remove bubbles and excess media. The mounted microscope slide is left in tinfoil overnight at room temp to allow for adequate curing of the mounting media. Once the media has completely cured, the microscope slide is carefully cleaned with ethanol to remove dirt and oil and is imaged using an AXIO Imager. A1m Fluorescent microscope (Carl Zeiss, Oberkochen, Germany) to determine cell adhesion and morphology.

Once the protocol for cell seeding has been shown successful, this protocol can be utilized to prepare cell seeded microscope slides for flow experiments. The general set up of the flow circuit and chamber is outlined in Figure 7. All flow experiments start by sterilizing the flow circuit and chamber in a Buxton steam autoclave (Buxton Co., Springfield MA) at 121 C for 60 mins. All flow components unable to be autoclaved due to the high temperature are sterilized using a UVO Cleaner model no. 342 (Jelight Company Inc., Irvine CA) for 10 mins to ensure the removal of cells or bacteria. Once the components of the flow experiment are sterile, they are moved into a laminar flow hood and the flow circuit is assembled (Figure 7A). 40 ml of TNF α media (5 ng/ml) is added to the media collection bottle using a sterile 60 ml syringe (Figure 7B), and the

circuit is assembled and placed in the incubator to allow the media to acclimate to the correct temperature (Figure 7C). While the media warms up in the incubator, the flow chamber can be assembled for the experiment. The top plate is assembled to the required tubing (Figure 7D), and a cell seeded microscope slide is placed into the bottom plate and covered with fresh media. The top and bottom plate are sealed with screws, and excess bubbles are removed by flushing the chamber with 10 ml of TNF α media.

The completed flow chamber assembly is now connected to the flow circuit and placed in the incubator with the rest of the circuit and media bottle (Figure 7E). The flow circuit tubing is connected to the pump and set at 65 RPM for 24 hours to allow for cell adaptation to flow. After the flow adaptation is complete, the cells can then be perfused with 250 ug/ml ICAM-Alexa-NP cell media for 4 hours under the same flow conditions. At specific time points, 1.5 ml of media is removed from the circuit and analyzed with a microplate reader to measure the level of fluorescence. The cell media fluorescence can be compared to the ICAM-Alexa NP fluorescent concentration curve to quantify the number of NPs in the cell media and give an indirect indication of the amount of NP attachment. After 4 hours of NP flow, the cell seeded slide is removed from the flow chamber and fixed, stained, and mounted in the same protocol listed above. The NP perfused microscope slide is then imaged using the AXIO scope, and the amount of Alexa 548 fluorescence is observed to confirm the attachment of the NPs.

To determine if the ICAM-NPs were able to bind under flow, an Alexa 568 conjugated secondary antibody is added in addition to the cell body and nuclei stain, which will bind to the ICAM antibodies on the surface of any bound NPs. The addition of this secondary antibody offers two advantages; first, having multiple Alexa 568

secondary antibody's bind to the surface of the NP will increase the amount of fluorescence seen in NP binding in comparison to the limited amount of Alexa 488 conjugated to the NP surface. It also allows us to use the cell body stain phalloidin 488, which would normally not be used as the fluorescence interferes with the Alexa 488 molecule conjugated to the ICAM-NPs. Being able to visualize the morphology of the cell body allows us to view where on the cell surface the NPs have attached and gives us a better understanding of the NPs ability to bind. With the combination of fluorescent imaging and cell media analysis, we will be able to determine if the ICAM NPs have the ability to bind under flow conditions.

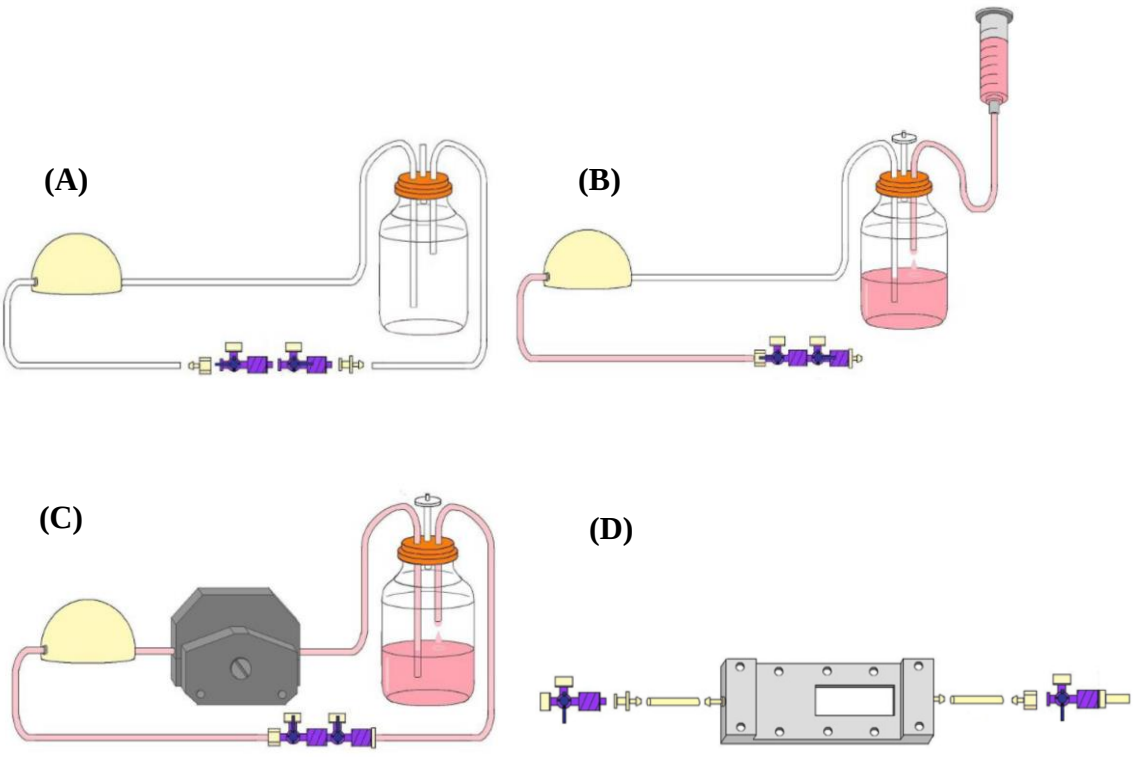

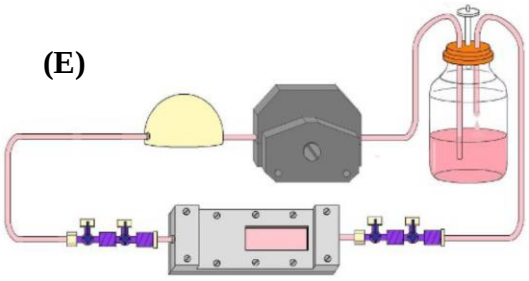

Figure 7. Schematic showing an overview of the flow circuit assembly and flow

experiment.

(A*) Assembled flow circuit after sterilization with stopcocks included. (B) Filling the glass reservoir with cell medium. (C) Flow circuit clamped into the flow pump head prior to flow chamber insertion. (D) Top chamber plate assembly. (E) Completely assembled flow circuit with inserted flow chamber during a flow experiment. Taken from Lane et al., J Vis. Exp (2012).*

Chapter III.

Results

The focus of this study was to create a targeted drug loaded PLGA-PEG NP and characterize the various properties of the NPs. To do this various cargo loaded NPs are generated and characterized, then applied to cell cultures under static or flow conditions. The various characterization techniques applied where chosen because each assay reveals information about the NP features that are essential for adequate drug delivery in the body. Since the time and budget constraints for this study excluded the possibility of in vivo experiments, the in vitro cell culture experiments provide vital information on the targeting properties of the NPs. The cumulative results from each of these experiments provides a preliminary examination of the feasibility of these NPs for a method of sustained drug delivery.

Size and Stability Characterization

The effectiveness of NPs as a platform for drug delivery is largely dependent on the NP formulation process. Thus, to study the effectiveness of the NP formation protocol, different characterization techniques are used to confirm each of the NPs essential properties. The size of the NPs can be evaluated using both DLS and SEM techniques. The data obtained from DLS size measurements gives the NPs average size based on three types of distributions; number, volume, and intensity (Table 1). A similar trend can be seen among all NP groups, where the average NP size increases from the number distribution, to the volume distribution, with the intensity distribution being the highest,

To confirm these DLS size results, each of the NP groups are imaged under a SEM to visualize the morphology and record the definite size of the NPs. As seen from Figure 8, the NPs are spherical in shape with a smooth surface. The genuine sizes of the NPs are obtained using an image processing program and can be compared to the DLS size results. Table 2 shows the average size and standard deviation of each NP group obtained from a number of sample measurements. The size measurements obtained from SEM images is most similar to the number distribution sizes of the DLS data, which confirms the accuracy of the DLS size data. The average size of the NP groups ranges from 120 to 150 nms, which is within the size range necessary for barrier penetration, which indicates the formulated NPs would be suitable for drug delivery to the blood stream (Yu et al, 2016).

The stability of the NP groups in solution is analyzed by measuring the NP group's zeta potential (Table 1). The formation of the PLGA-PEG NPs without additional cargo or surface modifications shows the most negative zeta potential which indicates the stability of the NP group, and an increase in zeta potential seen with all additional modifications. This change in zeta potential is to be expected as the addition of cargo or modification to the NP surface has been shown to alter the stability of the nanoparticles (Manoochehri et al., 2013).

Type	Number Distribution (nm)	Volume Distribution (nm)	Intensity Distribution (nm)	Zeta Potential (mv)
PLGA-PEG	142.8 +/- 14.6	146.8 +/- 15.8	152.0 +/- 16.6	-27.65 +/- 0.994
PLGA-PEG (Val)	154 +/- 39.9	200.5 +/- 78.8	332.7+/- 149.8	-7.99 +/- 4.506
PLGA-PEG (Cap)	138.3 +/- 31.9	170 +/- 55.8	234 +/- 74	-8.15 +/- 4.275
PLGA-PEG-ICAM	139 +/- 47.2	272.7 +/- 63.7	323.1 +/- 80.4	-12.5 +/- 4.753

Table 1. DLS Data:Size and Zeta Potential.

Results for the size and zeta potential tests using DLS techniques. Each of the NP groups used throughout the experiment are tested, and the mean and standard deviation of each result is listed. Size results are given for the number, volume, and intensity distribution generated from the analysis.

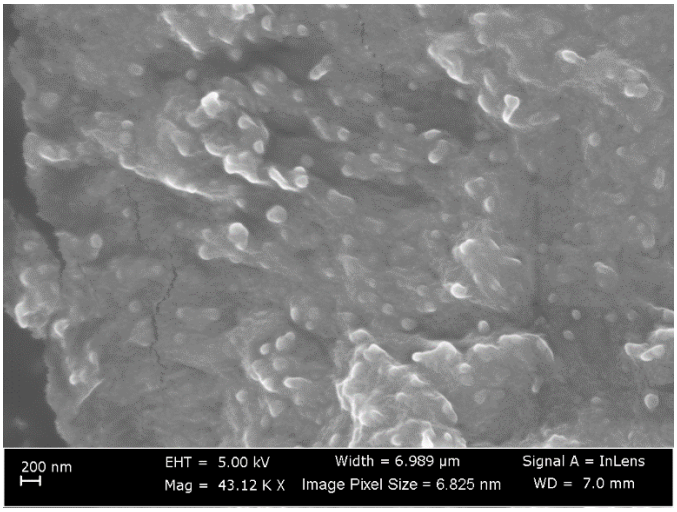

Figure 8. SEM Image of PLGA NPs.

Scanning electron microscopy used to visualize the morphology and size of PLGA NPs. Scale bar at bottom right lists the dimensions of the photo.

Group	Average Size (nm)	SD	# of Samples
PLGA-PEG	134.169	30.317582	67
PLGA-PEG (Val)	120.548	30.247255	96
PLGA-PEG (Cap)	147.358	32.275242	94
PLGA-PEG (ICAM)	118.487	22.726888	112

Table 2. Size analysis from SEM Image.

The real size of the various NP groups was obtained by measuring the size of the NPs in SEM images using Image J software. The mean and standard deviation, as well as the number of samples for each group is listed.

PEG Attachment Analysis

The addition of PEG molecules to the surface of the NP is essential for the NP to be able to navigate the bloodstream without being cleared away by the body's immune system. To confirm the PEG molecule attachment, both PEG modified PLGA NPs and unmodified PLGA NPs are analyzed using FTIR Spectroscopy. This technique works by shining a beam of light at a sample and measuring the amount of light the sample absorbs at each specific wavelength. Since different chemical structures produce different spectral fingerprints, it is possible to tell if PEG molecule has been successfully attached to the surface of the nanoparticle. Figure 9 shows the spectrum of the PEG-PLGA molecule, the blank PLGA NPs, and the subtraction of the PEG-PLGA spectrum from the PLGA spectrum. The subtracted spectrum shows clear differences between the PLGA-PEG and PLGA NP spectrums, which demonstrates a change in the structure of the molecule. If the PEG modification was unsuccessful, we would not see a difference between the PEG-PLGA spectrum and the PLGA spectrum. This is our first indication that the PEG modification was successful.

To ensure that the peaks seen in the difference spectrum is a result of the PEG attachment and not inference from other chemicals used during the PEG modification process, the PLGA spectrum is subtracted from the PEG-PLGA spectrum, and this difference spectrum can be compared to the spectrum of pure PEG molecules (Figure 10). We can see distinct spectrum peaks around 2900 cm^{-1} and 1200 cm^{-1} (indicated by the black arrows) which are similar to the PEG spectrum. This is another indication that the PEG modification process was successful, because we see aspects of the PEG only spectrum represented in the modified spectrum. An additional way of confirming that the

changes in the PEG-PLGA spectrum are due to the PEG molecule attachment, is by using the FTIR program's spectral library results. This library will compare the peaks of the collected spectrum (the PEG-PLGA minus PLGA spectrum) and try and find the best match of a known spectral peak. The spectral library (Figure 11) shows that the first three matches are for different Polyethlene Glycol (PEG) formulations, rather than any of the other chemicals used in the formulation process such as EDC or NHS. With the results of these three experiments, we can conclude that the PEG molecules were successfully attached to the PLGA NPs.

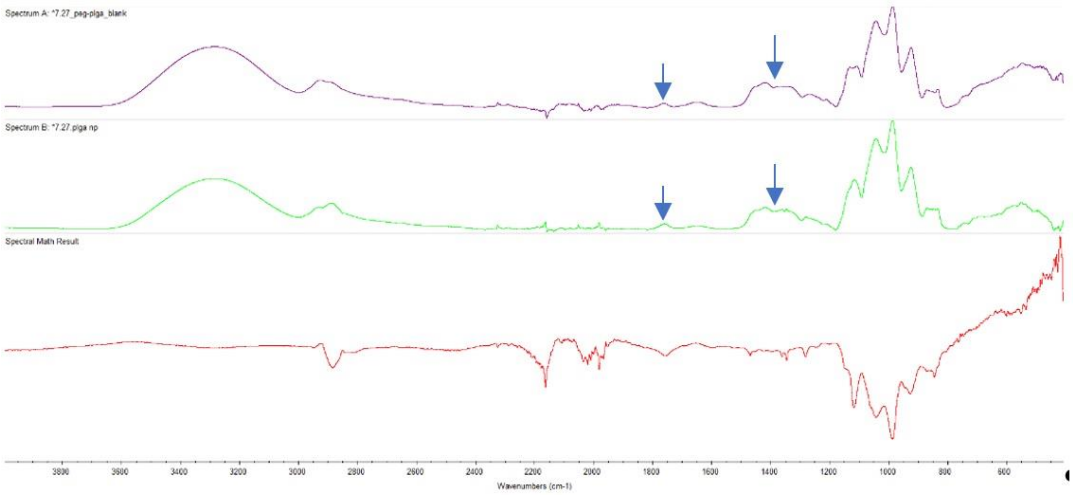

Figure 9. FTIR Spectrum: PLGA vs PEG-PLGA.

The FTIR spectrum of PLGA NP (top), PEG-PLGA NP (middle), and difference spectrum of the PLGA spectrum subtracted from the PLGA-PEG spectrum (bottom). The blue arrows indicate the peaks due to the absorbance of the C=O and CH3 functional groups of the PLGA polymer.

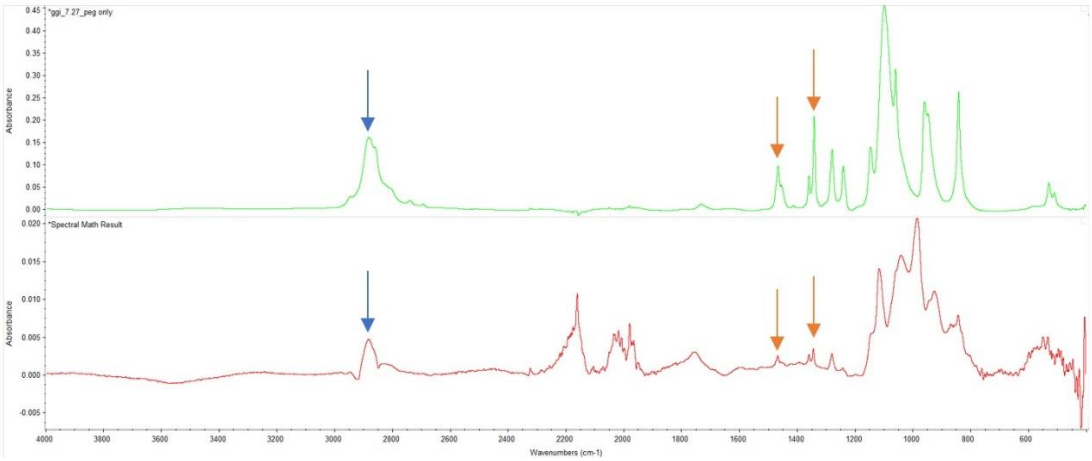

Figure 10. FTIR Spectrum: PEG vs Difference Spectrum.

The FTIR spectrum of the PEG only molecule (top) and the PEG-PLGA minus PLGA difference spectrum (bottom). The blue arrows indicate the peaks due to the -CH functional group, and the orange arrows indicate the peaks defined in both spectrums.

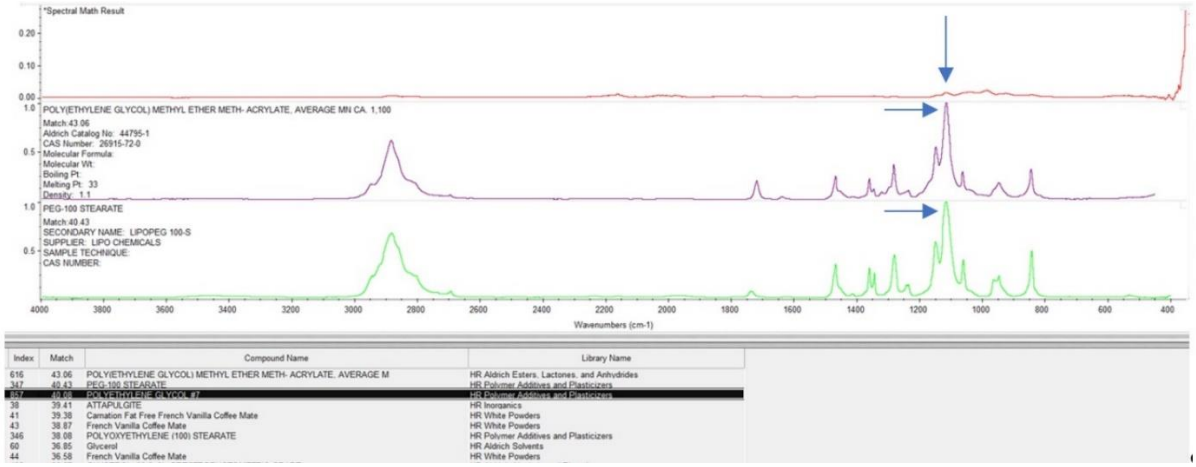

Figure 11. FTIR Spectrum: Difference Spectrum vs Spectrum Library.

The FTIR spectrum of the PLGA minus PEG-PLGA difference spectrum (top), the library spectrum for poly(ethylene glycol) acrylate (middle), and the library spectrum for PEG-100 (bottom). Blue arrows indicate the peaks characteristic of C-O stretching from the PEG molecule.

ICAM Antibody Attachment Confirmation

The surface of the PEG-PLGA NPs are modified with anti-ICAM antibodies, which is essential for the specific targeting of the NPs to lung microvascular cells. The success of ICAM antibody attachment can be confirmed by using a colorimetric pierce protein assay and the solution absorbance analyzed with a microplate reader. This assay is based on a dye-metal complex that binds to proteins in solution, resulting in a color change which can be quantified by measuring the change of absorbance. First a series of BSA protein dilutions are created to measure the amount of absorbance at a known protein concentration. These measurements can then be compared to the absorbance of a predetermined concentration of NPs in solution. To understand the amount of protein in solution, the absorbance of the BSA protein dilutions can be plotted against the BSA concentration, and a linear regression analysis of the plot gives us the equation for protein absorbance.

Figure 12 shows the measured absorbance for the average of 3 replicates of BSA standard solutions. The equation generated from the linear regression analysis has a high R squared value (0.9882), which demonstrates a highly linear correlation between BSA protein concentration and absorbance. This indicates that the absorbance values of the NP solutions will correspond to the correct amount of protein attachment. Using this standard curve, we can use the linear fit line equation to identify how much antibody has been conjugated to the PLGA NPs. We can see that for the unconjugated PEG-PLGA nanoparticle, there is a protein concentration of 9.36 ug, and for the ICAM conjugated PEG PLGA, there is a protein concentration of 50.56 ug (Table 3). After preforming a un paired t-test, we find that there is a statistically significant ($p = 0.0003$) difference

between the unconjugated and conjugated PEG PLGA NP, which indicates that the ICAM antibody was successfully attached to the NP.

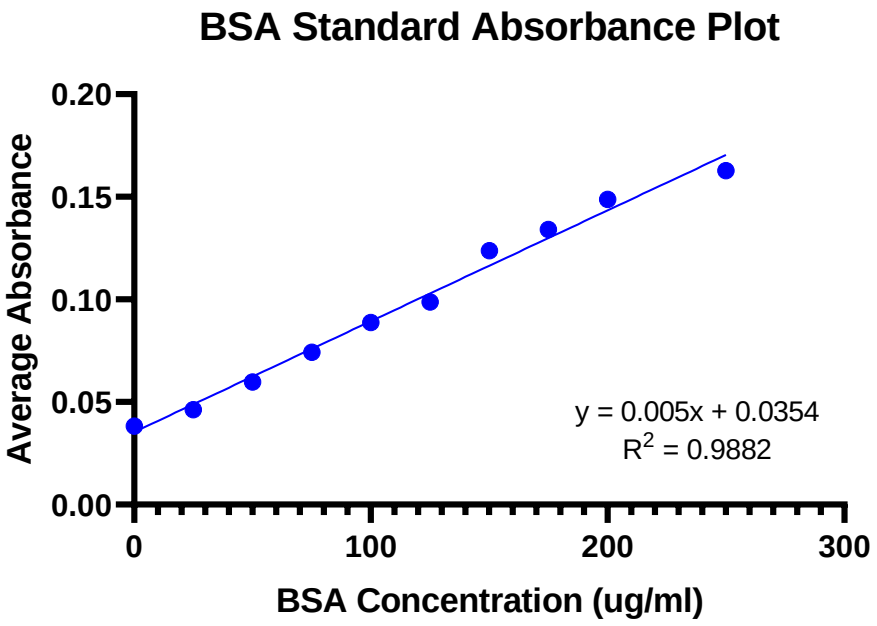

Figure 12. BSA Standard Absorbance Plot.

Measure of BSA absorbance at different concentrations of BSA in PBS (ug/ml). The plot shows a high degree of linearity (R^2=0.9882), with a linear regression equation of y=0.0005x + 0.0354. All samples were measured in triplicate and absorbance measured at 660 nm.

Group Type:	Absorbance Intensity	Raw Protein (ug/ml)	Standardized Protein (ug/ml)
PLGA-PEG-ICAM-1	0.063 +/- 0.004	55.2	50
PLGA-PEG	0.041 +/- 0.000	11.2	6
BSA Test (0 ug)	0.038 +/- 0/001	5.2	0

Table 3. Absorbance Comparison of PLGA-PEG ICAM NPs vs PLGA-PEG NPs.

Average measure of absorbance (with standard deviation) of the PLGA-PEG ICAM vs PLGA-PEG NPs. The absorbance is converted to protein concentration using the linear regression equation from Figure 12. This protein concentration is standardized by removing the protein concentration seen at 0 ug/ml BSA. All samples are measured in triplicate and absorbance measured at 660 nm.

Alexa Attachment Confirmation

To attachment of Alexa 488 fluorescent molecules to the surface of the NPs is essential for the ability to visualize the NPs during cell binding experiments. To confirm the attachment of the fluorescent molecule, both unconjugated and Alexa conjugated PEG-PLGA NPs are dispersed at the same concentration in distilled H20 and analyzed for fluorescence with a microplate reader. The level of fluorescence of the Alexa NPs is significantly higher than the fluorescence of the unconjugated NPs ($p < -0.0001$), which indicates that the Alexa molecule was successfully attached to the surface of the NP (Table 4).

Once the attachment of the Alexa molecule to the NP has been confirmed, it is important to understand how much of the Alexa molecule has been attached to the NP, and to confirm that this fluorescence can be identified when the NPs are dispersed in cell medium instead of H20. To understand the amount of Alexa 488 attached to the NP, first a standard curve of the Alexa 488 molecule must be performed to correlate level of fluorescence to Alexa 488 concentration. Figure 13 shows the amount of fluorescence for varying concentrations of Alexa 488, and the regression analysis of this plot demonstrates that the Alexa 488 standard curve has a highly linear fit ($R^2= 0.9996$), indicating that amount of fluorescence can accurately determine Alexa 488 concentration.

The Alexa 488 standard curve can be used to determine the amount of Alexa 488 conjugated to the NPs. By determining the amount of Alexa-488 per milligram of NP

solution, we will be able to determine the concentration of NP in solution using fluorescent analysis alone. This experiment is essential, as fluorescent analysis of Alexa-NPs in cell media will be used to quantify the amount of NP binding during flow experiments. To determine the amount of Alexa-488 and conjugated to the NPs, a range of Alexa-ICAM conjugated NP concentrations are diluted in cell media and measured for amount of fluorescence. The concentration curve for the Alexa+ICAM NP fluorescence shows a high level of linearity (R^2= 0.989), indicating that the concentration of Alexa+ICAM NP can be determined based on the NP solution (Figure 14).

Group Type:	Fluorescent Intensity: (average)
PLGA-PEG (Alexa)	694.35
PLGA-PEG	15.703
Water	-4.235
Air	0.0003

Table 4. Fluorescent Intensity of PLGA-PEG (Alexa) vs PLGA-PEG.

The average fluorescence intensity of PLGA-PEG (Alexa) compared to PLGA-PEG. Fluorescence measurements for water and air are included for use in standardizing results. All samples are measured in triplicate, and excited at 488 nm and fluorescence intensity measured at 530 emission.

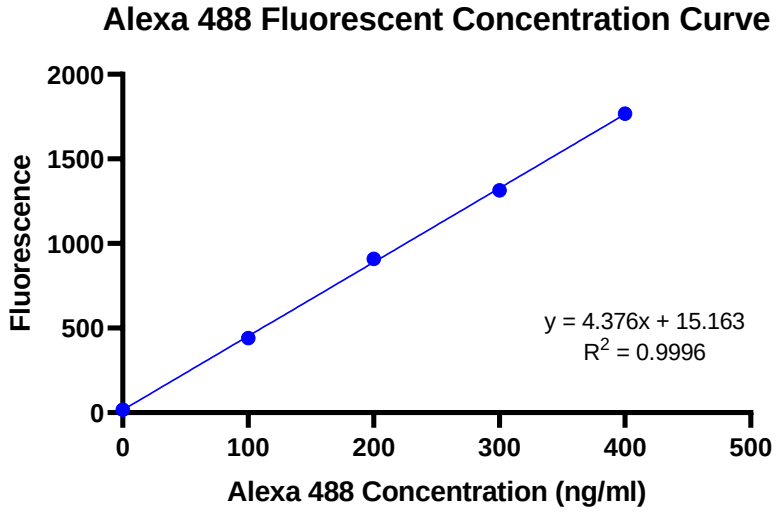

Figure 13. Alexa 488 Fluorescent Concentration Curve.

Measure of Alexa 488 fluorescence intensity at different concentrations of Alexa 488 in cell media (ng/ml). The plot shows a high degree of linearity (R^2=0.9996), with a linear regression equation of y=4.3736x +15.163. All samples were measured in triplicate and excited at 488 nm and fluorescence intensity measured at 530 emission.

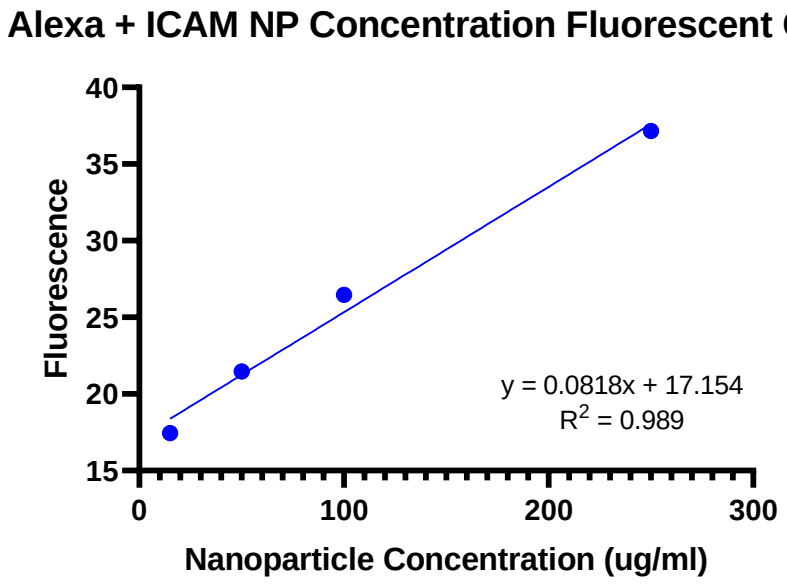

Figure 14. PLGA-ICAM-Alexa NP Fluorescent Concentration Curve.

Measure of PLGA-ICAM-Alexa NP fluorescence intensity at different concentrations of NPs in cell media (ug/ml). The plot shows a high degree of linearity (R^2=0.989), with a linear regression equation of y=0.0818x +17.154. All samples were measured in triplicate and excited at 488 nm and fluorescence intensity measured at 530 emission.

Drug Loading and Release Analysis

The drug loading and drug release of Valsartan and Captopril from the ICAM-NPs are studied to understand the NP's ability to provide a sustained drug release. The final drug loading and encapsulation efficiency for each of the drugs is listed in Table 5. The values for drug concentration are obtained by comparing the absorption values of the

acetonitrile/methanol supernatant to the linear regression equations obtained based on the drug calibration curve in the same solution (Figure 15, Figure 16). Each of the calibration curves has a high degree of linearity (R^2 >0.95) so we can be sure the concentration values generated from the equations are accurate. We see that for both drug loading and encapsulation efficiency, Captopril has a higher percent than Valsartan, which means the drug was easier to encapsulate into the NP. However, since both NP formulations are able to encapsulate some amount of drug, the timeline of the release for each drug can be studied.

Since the UV-VIS absorbance of drug can changed based on the solution, additional calibration curves for each drug must be created to be able to characterize the drug release results. Figure 17 and Figure 18 demonstrate the high degree of linearity for each standard curve (R^2>0.98) which indicates the accuracy of the curve in this alternate medium. Once the calibration curve has been established, the linear regression equations are used to calculate the concentration of the drug release at various time points, and the amount of drug released over time can be observed (Table 6). Since Captopril NPs display a higher encapsulation efficiency than Valsartan NPs, the overall amount of drug released is significantly higher. Data points were taken until the amount of drug release did not show any significant increase, indicating the total amount of drug was released from the NPs. Once the total amount of drug release is determined, these results can be displayed to understand the timeline for percent of drug release (Figure 19, Figure 20). Valsartan NPs have an initial burst release of drug during the first four hours, where 15% of the encapsulated drug is released, while Captopril displays a much smoother release rate, having only 2% released in the first 4 hours. Both drugs have released 100% of their

drugs by 100 hours, which is almost 4 days. These results demonstrate that both Captopril and Valsartan loaded drugs are capable of sustained drug release

Drug	Amount of NP	Total Amount of Drug added	Amount of Drug in NP	Drug Loading %	Encapsulation Efficiency %
Valsartan	15 mg	3.6 mg	1.1139 mg	7.426	30.942
Captopril	15 mg	3.6 mg	2.3314 mg	15.5427	64.759

Table 5. Drug Loading and Encapsulation Efficiency of Valsartan and Captopril.

The results for drug loading and encapsulation efficiency for both valsartan and captopril. Each of the variables needed to calculate these equations are included as well; amount of NP used, total amount of drug added, and amount of drug in NP. These results are obtained based on the linear regression equations generated from the Figure 14 and Figure 15.

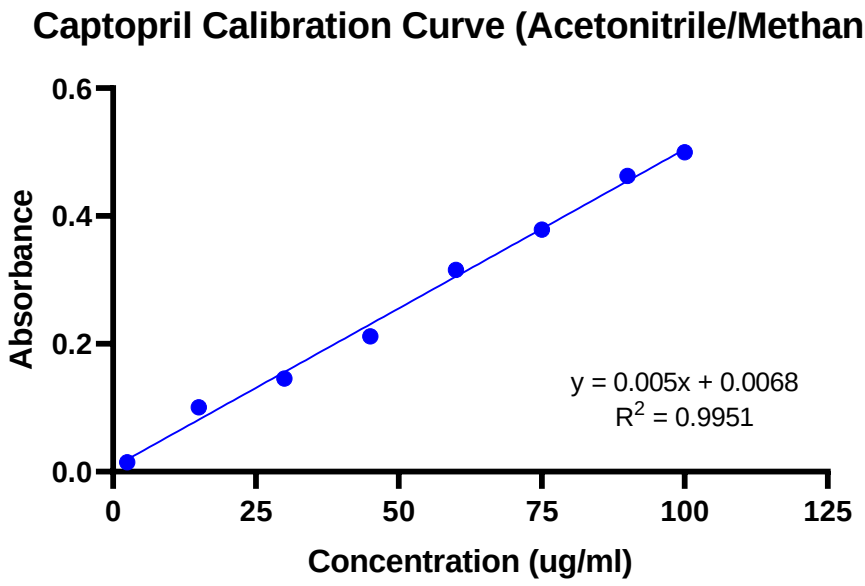

Figure 15. Captopril Calibration Curve in Acetonitrile and Methanol.

Measure of Captopril absorbance at different concentrations of the drug dissolved in a 1:5 ratio of acetonitrile and methanol (ug/ml). The plot shows a high degree of linearity (R^2=0.9951), with a linear regression equation of y=0.005x +0.0068. All samples were measured in duplicate and absorbance measured at 210 nm.

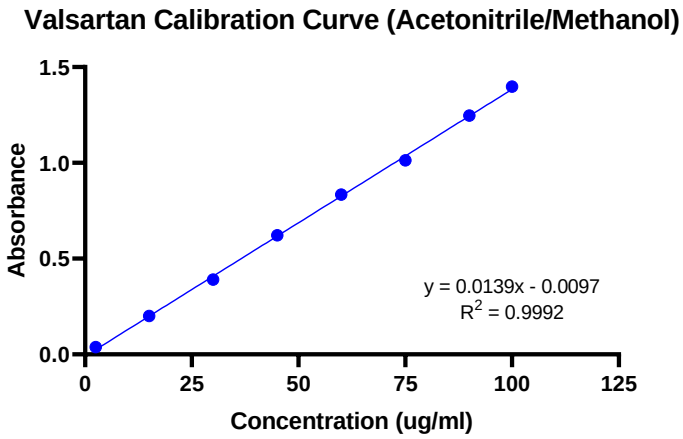

Figure 16. Valsartan Calibration Curve in Acetonitrile and Methanol.

Measure of Valsartan absorbance at different concentrations of the drug dissolved in a 1:5 ratio of acetonitrile and methanol (ug/ml). The plot shows a high degree of linearity (R^2=0.9992), with a linear regression equation of y=0.0139x +0.0097. All samples were measured in duplicate and absorbance measured at 205 nm

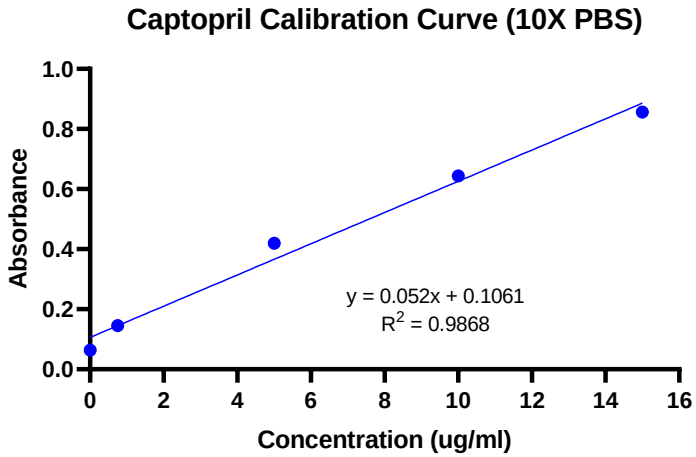

Figure 17. Captopril Calibration Curve in 10X PBS

Measure of Captopril absorbance at different concentrations of the drug dissolved in a 10x PBS (ug/ml). The plot shows a high degree of linearity (R^2=0.9868), with a linear regression equation of y=0.052x +0.0161. All samples were measured in duplicate and absorbance measured at 210 nm.

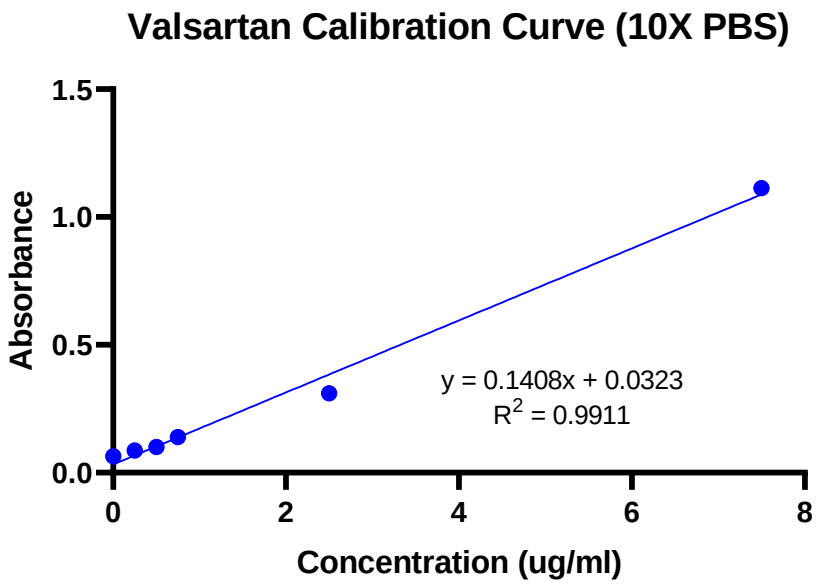

Figure 18. Valsartan Calibration Curve in 10X PBS.

Measure of Valsartan absorbance at different concentrations of the drug dissolved in a 10x PBS (ug/ml). The plot shows a high degree of linearity (R^2=0.9911), with a linear regression equation of y=0.1408x +0.0323. All samples were measured in duplicate and absorbance measured at 205 nm.

Timepoint (hours)	4	24	48	72	105	142
Amount of Valsartan Released (ug)	99.70	125.48	350.88	547.51	660.86	661.82
Amount of Captopril Released (ug)	36.99	179.37	603.19	1527.26	1698.58	1703.95

Table 6. Total Drug Release (ug) of Captopril and Valsartan.

The average amount of Valsartan and Captopril (ug) over a period of time to measure drug release. These drug values were obtained by measuring the absorbance at each time point and converting it to drug concentration using linear regression lines from Figure 16 and Figure 17. Each sample was measured in duplicate, and total drug release was calculated based on the volume of sink media and the drug amounts from the samples removed for analysis.

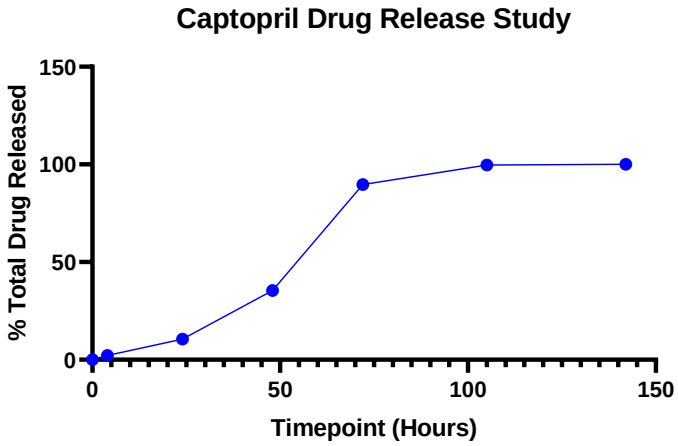

Figure 19. Captopril % Total Drug Release Timeline

The percent of total drug release of Captopril is recorded for each time point. The total amount of drug was taken as the drug amount value at the last timepoint, when it was determined there was no significant change in drug release.

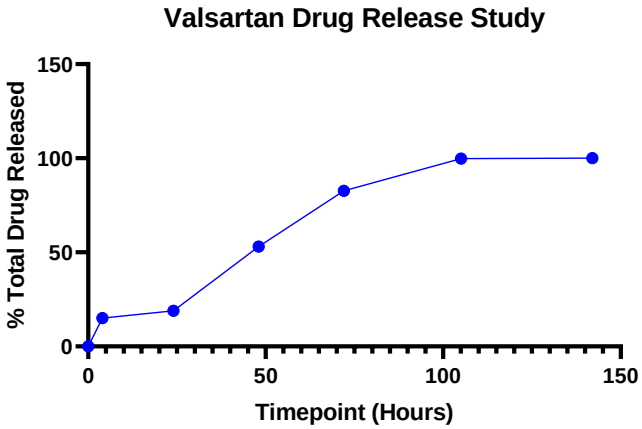

Figure 20. Valsartan % Total Drug Release Timeline.

The percent of total drug release of Valsartan is recorded for each time point. The total amount of drug was taken as the drug amount value at the last timepoint, when it was determined there was no significant change in drug release.

Static NP Binding Experiments

The modification of the surface of the NP with the anti-ICAM antibody allows the surface to target and bind to specific cell areas. The anti-ICAM target allows the NP to bind to pulmonary vascular cells that have upregulated amounts of ICAM receptors due to hypertensive condition (Muzykantov, 2013). To mimic the upregulation of ICAM receptors seen in these conditions, the cells used for the experiment are activated with TNF α (an inflammatory agent). The correct concentration of TNF α to increase ICAM receptor density is tested by evaluating the level of anti-ICAM antibody fluorescence displayed after 24 hours of specific TNF α concentrations. Figure 21 demonstrates the ability of TNF α to increase the receptor density. Although there is a small amount of fluorescence seen at 0 ng/ml, the difference between that and the 5 ng/ml and 10 ng/ml shows an extremely high level of significance ($p<0.0001$), which shows that the fluorescence seen at those concentration ranges isn't due to nonspecific binding of the fluorescent antibody. Figure 22 shows the fluorescent and brightfield images of each concentration range, and it's clear based on the overlay images that the anti-ICAM fluorescence is congregated around the nucleus and cell body, not the well plate. This demonstrates the ability of TNF α to increase ICAM receptor density on the surface of the HUVECs. Since the difference in fluorescent intensity between the 5 ng/ml and 10 ng/ml group wasn't found to be significant ($p=0.2284$), 5 ng/ml was chosen as the final TNF α concentration for future cell binding experiments.

Once the ideal concentration of TNF α is chosen for ICAM receptor upregulation, the concentration of NPs is evaluated for level of binding. Different concentrations of NP solutions are incubated for two hours with TNF α activated HUVECS and the level of

fluorescent intensity is measured for each group. To ensure the NP binding that occurs is due to the ICAM antibody and not the NP itself, the fluorescent intensity is compared for Alexa NPs and ICAM+NPs at the same concentration ranges for the same amount of time (Figure 23)**.** The Alexa-NPs did not show any statistically significant difference in binding for the 15 ug/ml compared to the control ($p=1.1970$), however the higher concentration ranges (50 ug/ml, 100 ug/ml, 250 ug/ml) showed significant differences ($p=0.0373$, $p=0.002$, $p= 0.0001$). This indicates a certain amount of NP binding occurs despite the absence of the anti-ICAM NP. However, when comparing the fluorescent intensity of the 50 ug/ml group to the higher concentration ranges (100 ug/ml, 250 ug/ml), no significant differences were found between the groups ($p=0.0714$, $p=0.8197$), which indicates that amount of binding does not increase with Alexa-NP concentration. Figure 24 shows the level of fluorescent for each Alexa NP group, and it's clear to see that the amount of NP binding does not significantly increase as the concentration increases.

The ICAM conjugated NPs displayed a much larger change in fluorescent intensity through all NP concentration groups. The amount of fluorescent intensity is significantly higher for each NP formation group in comparison to the control ($P<0.0003$), which indicates the fluorescent intensity seen in each group isn't due to nonspecific fluorescent binding. The highest concentration range (250 ug/ml) displayed significantly increased level of binding compared to the 15 ug/ml, 50 ug/ml, and 100 ug/ml concentration groups low ($p<0.0001$, $p<0.001$, $p=0.0436$), indicating that the amount of NP binding increased with NP concentration. By observing the converged fluorescent and brightfield images of the ICAM-NP binding groups (Figure 25), you can

see that each of the ICAM-NP binding sites occurs on the surface of the cell, which demonstrates the actual cellular NP binding instead of binding to the plate surface. Although there we can see an increase in fluorescent intensity as both Alexa-NP and ICAM-NP concentration increases, there is a statistically significant difference between the fluorescent intensity of the two groups at each of the NP concentrations ($p<0.0001$), which demonstrates the increased ability of the NP to bind to the cell with the addition of the anti-ICAM antibody.

Once the ideal NP concentration is identified, the timeline for ICAM-NP binding can be studied to understand how fast the ICAM-NP can bind to activated HUVECS. 250 ug/ml of ICAM-NP solution is incubated for different periods of time, and the fluorescent intensity of each group is recorded (Figure 26). Compared to the fluorescent intensity of the 0 mins control group, each of the NP timeline groups showed significant increases in fluorescent intensity ($p<0.05$), which demonstrates the ability for the ICAM-NP to bind in as little as 30 mins. Although there wasn't a significant change in fluorescent intensity between 30 and 60 mins ($p=0.09367$), the amount of fluorescence significant increases between each of the timepoints after that ($p<0.05$). This indicates that the ICAM NP's are continually bind as the amount of time in contact with the cells increases. Figure 27 shows the location of the ICAM-NP binding, demonstrating the adhesion of the NPs to the cell body rather than the well surface.

One of the reasons the anti-ICAM antibody was selected as the targeting antibody for this study is due to the fact that the ICAM receptor is only upregulated in activated cells, which would limit the amount of nonspecific binding to non-activated cells in other areas of the body. To test the binding specificity of the NP, 250 ug/ml of either ICAM-

NP or Alexa-NP are incubated for 4 hours with either TNF α treated cells or normal media treated cells. The fluorescent intensity of each group can be compared to determine the amount of nonspecific binding (Figure 28). There is a significant increase in fluorescent intensity between the ICAM NP active group and the ICAM NP unactivated group ($p<0.0001$), which demonstrates the NP's increased binding abilities to activated vs unactivated HUVECS. However, there is a slightly significant difference between the fluorescent intensity of the ICAM unactivated NP group and the control group, which indicates there is some amount of ICAM NP binding occurring on the surface of the unactivated HUVECS. When comparing the fluorescent intensity of the activated and unactivated Alexa NP groups, we don't see any significant changes in the intensities ($p=0.9531$), which indicates the binding preferences of unconjugated NPs are the same for unactivated and activated cells. With the culmination of these experiments, it clear that the ICAM-NPs demonstrate the ability to bind to the surface of the HUVEC cells.

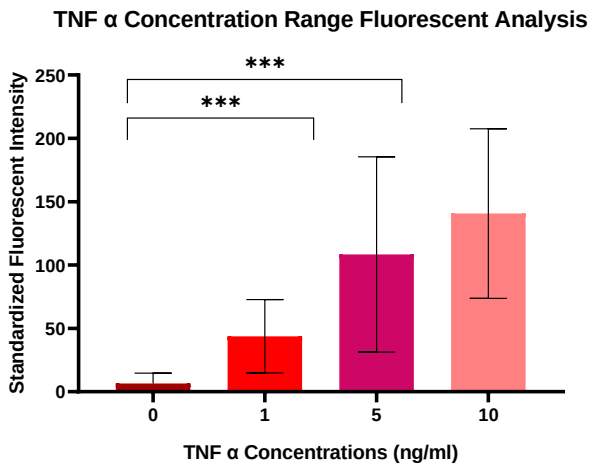

Figure 21. Fluorescent Analysis of TNF α Concentration Range.

The average anti-ICAM florescent intensity for different concentrations of TNF α treatment (ng/ml). Fluorescent intensity is measured using Image J software and standardized against background fluorescent intensity. A minimum of 30 cells are measured and stand deviation of the groups displayed.

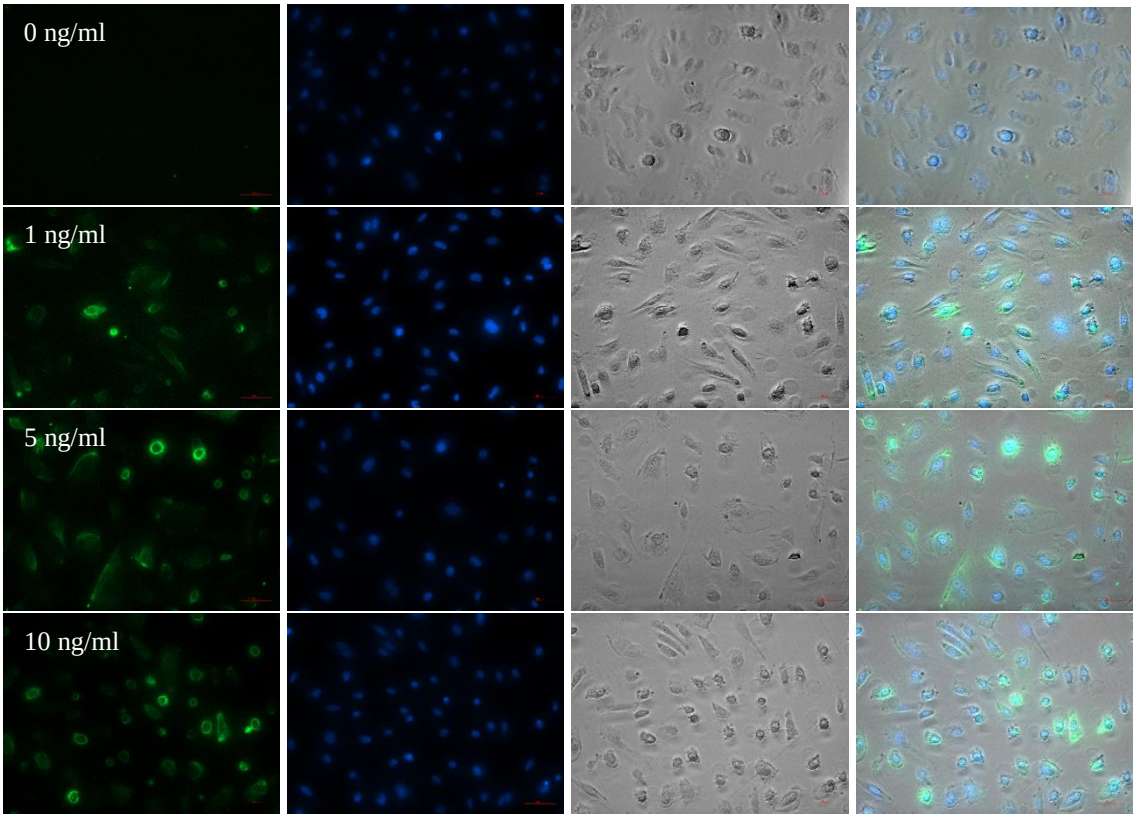

Figure 22. Fluorescent Images of TNF α Concentration Range.

Images from each fluorescent channel at different TNF α concentration treatments. Images include Hoechst stains for the nuclei (blue), and Alexa 488 secondary antibody for ICAM receptors (green), brightfield image of the cells, and the merged channel image. All samples are imaged at the same LED power and exposure to allow for comparison of fluorescent intensity. Scale bar measures 50 um.

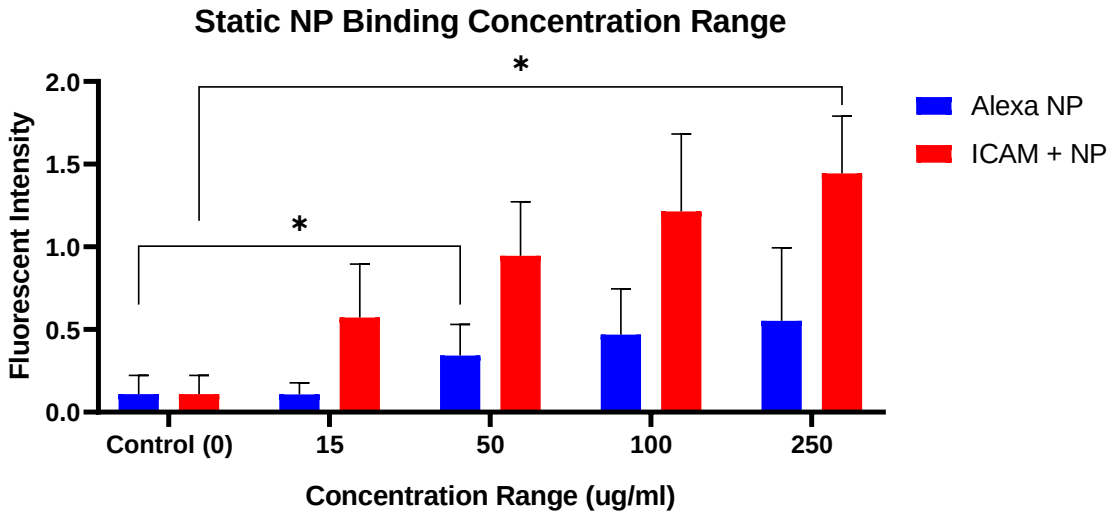

Figure 23. Fluorescent Analysis of ICAM-NP and Alexa NP Concentration Range.

The average florescent intensity of Alexa NP and ICAM-NP for different concentrations of NP (ug/ml). Fluorescent intensity is measured using Image J software and standardized against background fluorescent intensity. A minimum of 30 cells are measured and stand deviation of the groups displayed.

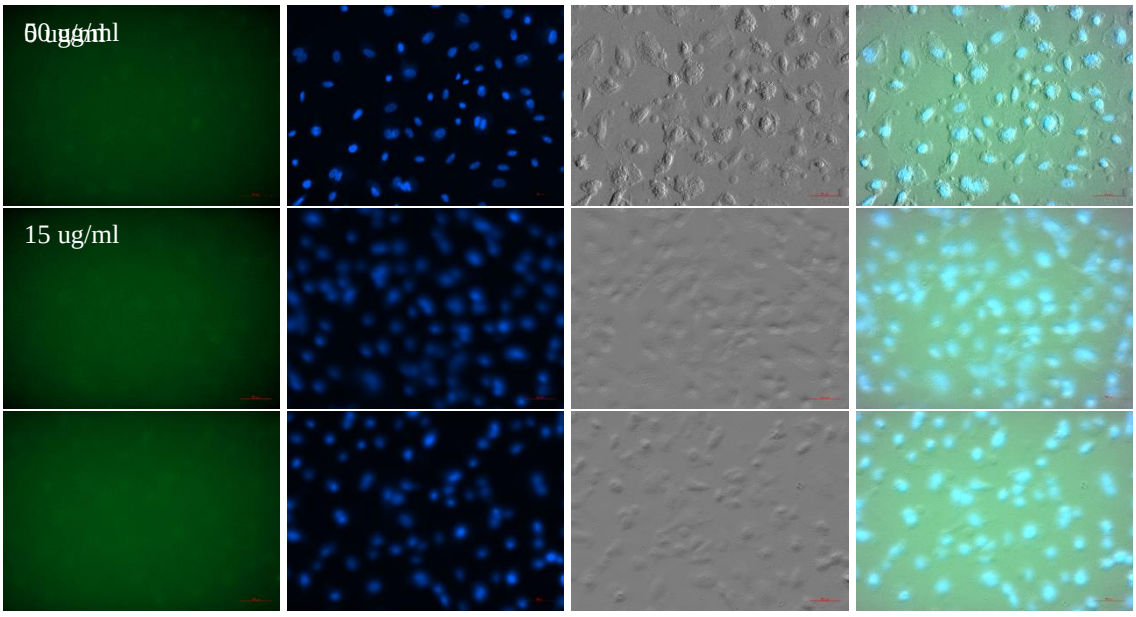

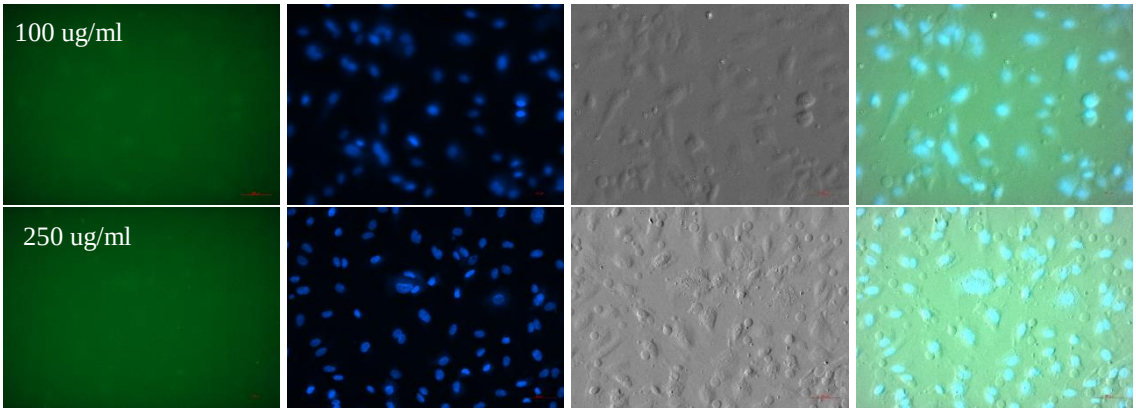

Figure 24. Fluorescent Images of Alexa-NP Concentration Range.

Images from each fluorescent channel at different Alexa-NP concentration treatments. Images include Hoechst stains for the nuclei (blue), Alexa 488 NPs (green), brightfield image of the cells, and the merged channel image. All samples are imaged at the same LED power and exposure to allow for comparison of fluorescent intensity. Scale bar measures 50 um.

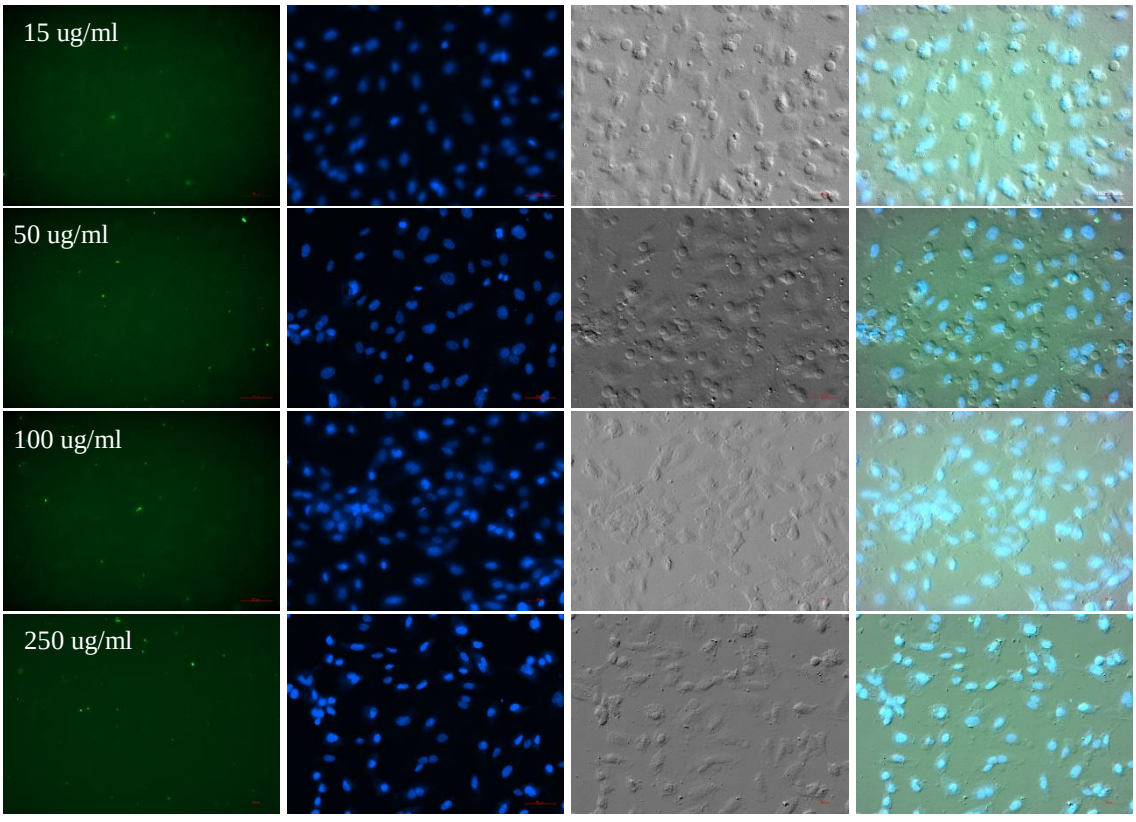

Figure 25. Fluorescent Images of ICAM-NP Concentration Range.

Images from each fluorescent channel at different Alexa ICAM-NP concentration treatments. Images include Hoechst stains for the nuclei (blue), Alexa ICAM NPs (green), brightfield image of the cells, and the merged channel image. All samples are imaged at the same LED power and exposure to allow for comparison of fluorescent intensity. Scale bar measures 50 um.

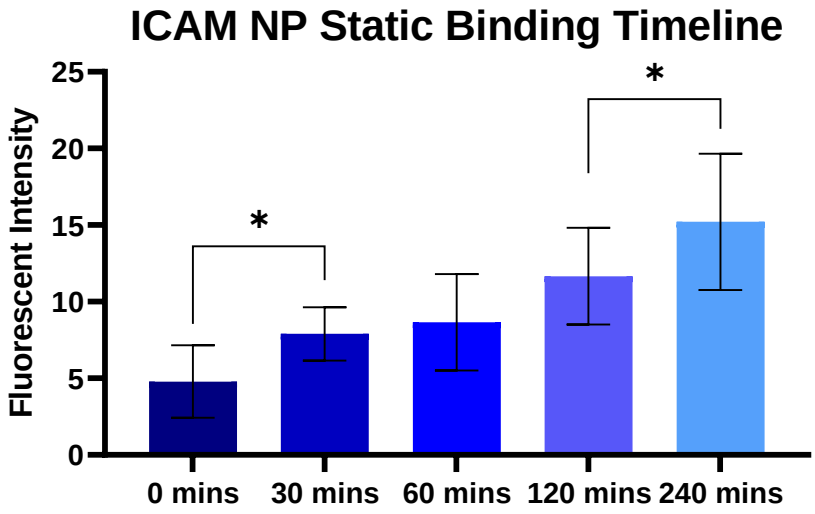

Figure 26. Timeline of Fluorescent Intensity for ICAM-NP Static Binding.

The average florescent intensity of ICAM-NPs for different incubation times. Fluorescent intensity is measured using Image J software and standardized against background fluorescent intensity. A minimum of 30 cells are measured and stand deviation of the groups displayed.

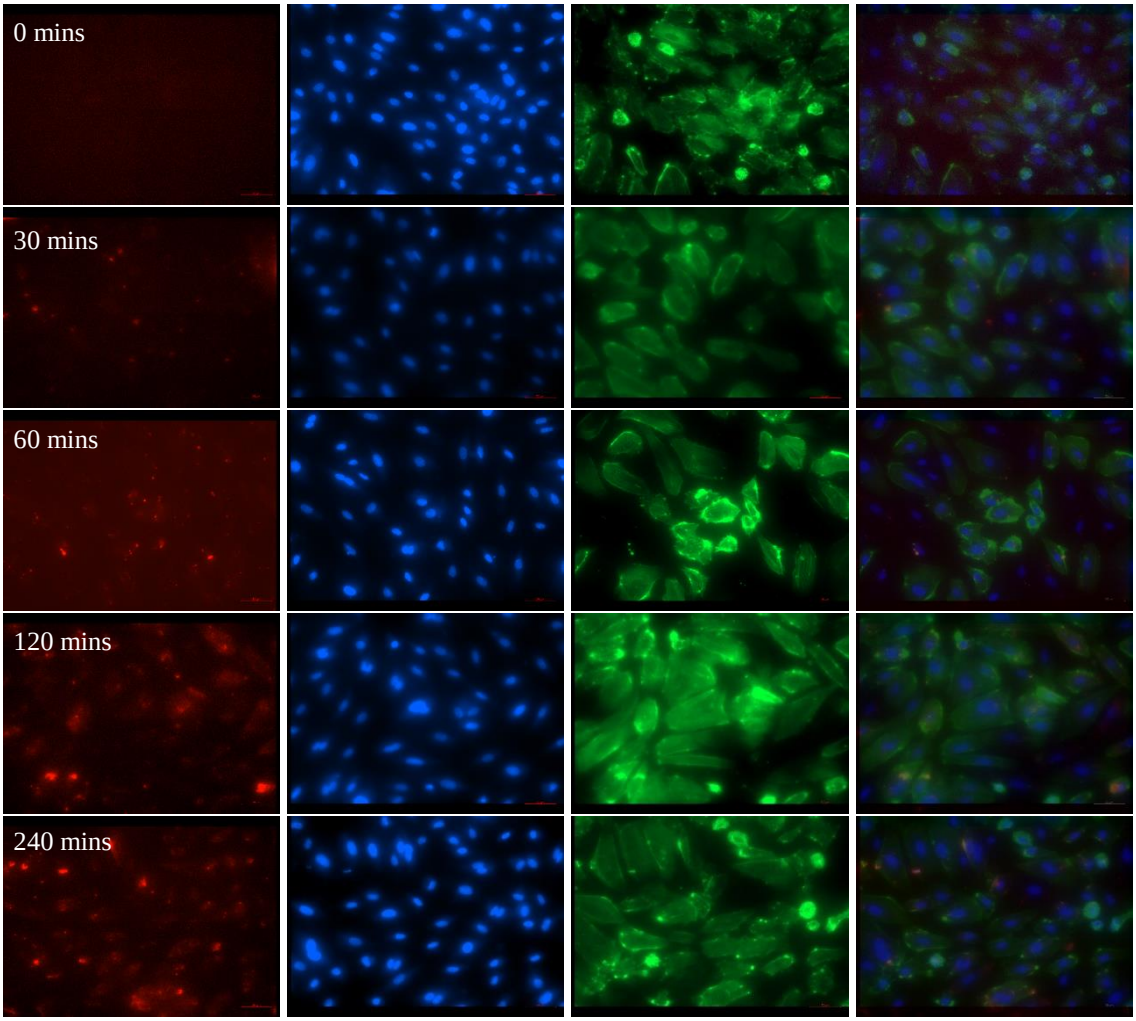

Figure 27. Fluorescent Images of Timeline of ICAM-NP Static Binding.

Images from each fluorescent channel at different timepoints of ICAM-NP binding. Images include Hoechst stains for the nuclei (blue), Alexa 568 secondary antibody for ICAM NPs (red), phalloidin 488 for the cell body (green), and the merged channel image. All samples are imaged at the same LED power and exposure to allow for comparison of fluorescent intensity. Scale bar measures 50 um

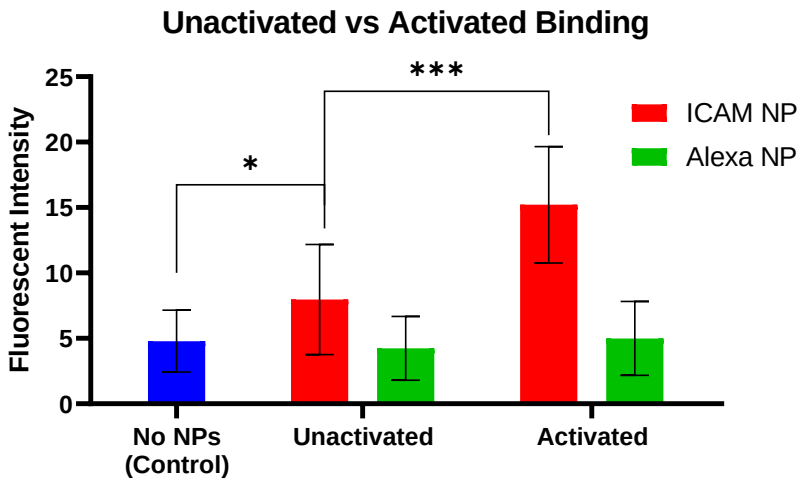

Figure 28. Fluorescent Intensity of NP Binding to Unactivated or Activated HUVECs.

The average florescent intensity of ICAM-NP and Alexa-NPs for 4 hours to TNF α treated or normal media HUVECS. The fluorescent intensity of the control group (no NP binding) was used to determine background fluorescent intensity. Fluorescent intensity is measured using Image J software and standardized against background fluorescent intensity. A minimum of 30 cells are measured and stand deviation of the groups displayed.

Flow Experiment

The previous experiments demonstrated the ability of the ICAM NP to bind to activated HUVECs. However, these experiments were performed under static conditions, and it's been shown that the introduction of shear stress can affect the binding abilities of antibody conjugated NP's (Calderon et al., 2009). Since these NPs are designed to target the cell wall of blood vessels, it is essential that they also have the ability to bind even under the force of shear stress. To understand how the binding capacity of the ICAM NP changes during flow conditions, HUVECs are seeded onto fibronectin coated slides and inserted into the designed flow chamber. Before proceeding with flow experiments, the

binding capacity of the HUVECs to the fibronectin coated glass slides must be assessed. Fluorescent images were taken after 24 hours of cell adherence to fibronectin coated slides (Figure 29). We can see based on the cell body and nuclei stains that the cells present a high level of density and a good morphology, both of which are essential for the following flow experiments. These images are a good indication that the fibronectin protocol used is adequate for cell adherence and can be used for the cell seeding procedures for flow experiments.

Once the cell binding to microscope slides has been confirmed, the cells can be placed into the flow chamber and adapted overnight with TNF α media at the specified flow rate. The cells are introduced to flow conditions for a length of time before NPs are introduced to allow the cells to adapt to flow conditions and to display the morphology and physiological conditions seen in flow. These flow adaptations are essential for the NP binding experiments, as the characteristics of cells under flow can be drastically different than those in static conditions (Bhowmick et al., 2012). After the cells have been adapted to the selected flow rate, 250 ug/ml of ICAM-Alexa-NPs are introduced into the flow circuit and allowed to perfuse the chamber for four hours. At selected time points, media is withdrawn from the flow chamber and analyzed for amount of fluorescence. This fluorescence can be converted to ICAM-NP concentration using the linear regression curve generated from the ICAN-NP concentration curve (Figure 14)**.** There is a significant difference between the control timepoint (0 hours) and all further timepoints ($p<0.0001$), which indicates the appearance of the fluorescent NPs and further confirms the ability of the test to detect NPs in media (Figure 30). However, no significant differences were found between the NP binding timepoints, which would initially suggest

that the NP's were unsuccessful at binding to the HUVECS under flow. However, since the final concentration of NP's at the 4-hour time point is less than the initial concentration added (220 ug/ml vs 250 ug/ml), there is a chance that there is a small amount of binding occurring which would reduce the final conc on NPs in the media. To further investigate these results, the cell microscope slide is removed after the NP binding experiment, and fixed and stained for fluorescent imaging.

Since an Alexa 568 secondary antibody is included during the florescent staining, we should be able to visualize any bound nanoparticles present on the surface of the cells. Figure 31 shows specific points of red fluorescence present on the surface of the cells, which could be an indication of NP binding. To ensure the red fluorescence present in these images is not due to non-specific binding of the Alexa 568 secondary antibody, an additional experiment is performed with cells placed in the flow chamber and adapted to 24 hours of TNF α flow. These cells are immediately removed from the chamber, and fixed and stained using the same procedure as the NP flowing binding experiment. The cells are imaged at the same LED power and exposure as the previous experiment to determine the amount of secondary antibody non-specific binding (Figure 32). These images show very low levels of red fluorescence present, which would indicate that the secondary antibody is not bound to the cells or surrounding areas at the same level as seen in Figure 31. These results lead us to the conclusion that the red fluorescence seen in Figure 28 are due to the secondary antibody binding to the ICAM antibody on the surface of the NPs, and this would indicate the ability of the NPs to bind under flow conditions.

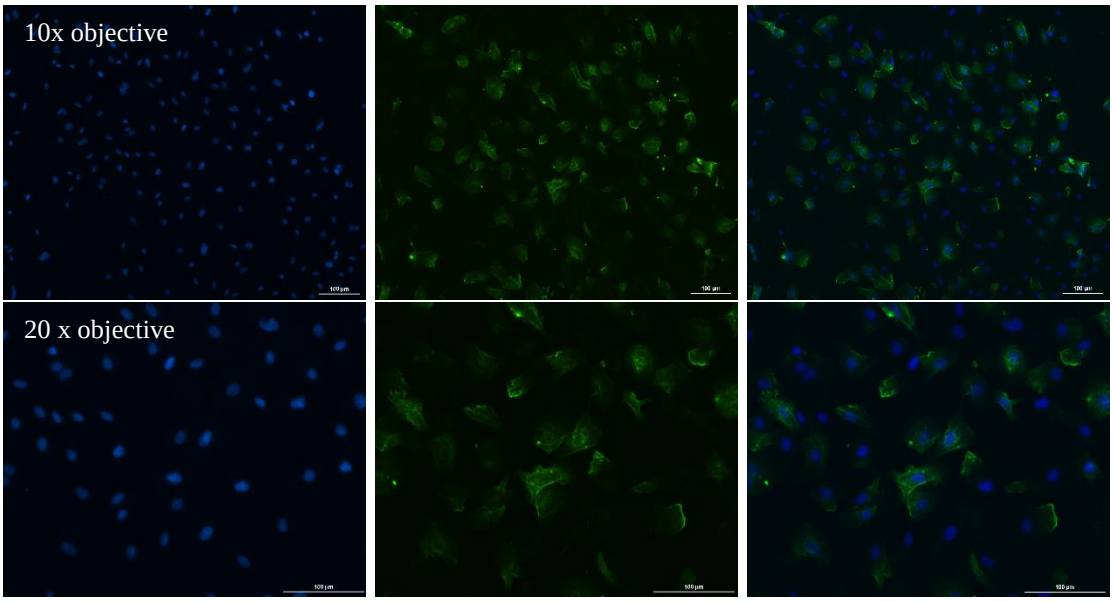

Figure 29. Fluorescent Images of HUVECs on Microscope Slide.

Images from different fluorescent channels taken from HUVEC seeded onto 5 ug/ml fibronectin coated slide. Images include Hoechst stains for the nuclei (blue), phalloidin 488 for the cell body (green), and the merged channel image. All samples are imaged at the same LED power and exposure to allow for comparison of fluorescent intensity. Scale bar measures 100 um.

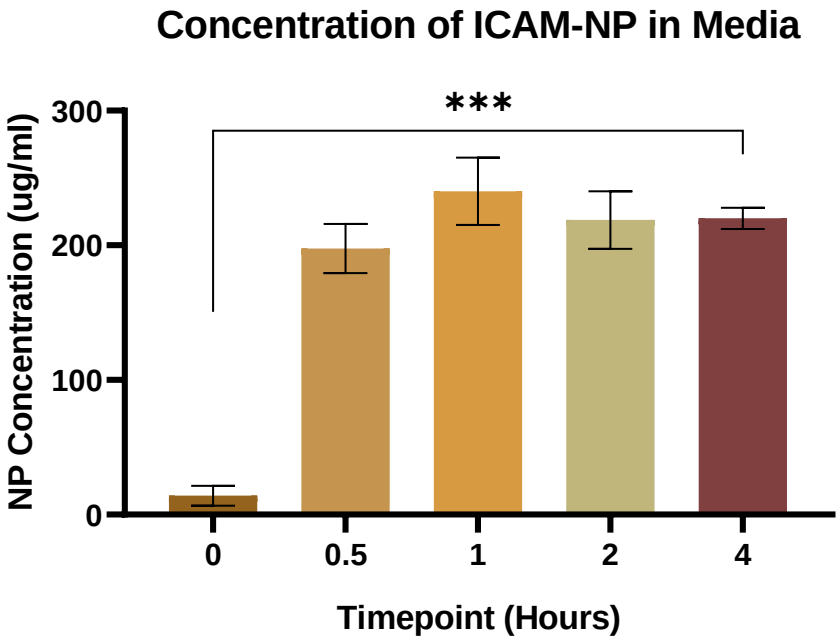

Figure 30. NP Concentration of ICAM NP in Cell Media from Flow Experiment.

The average NP concentration (ug/ml) of ICAM-NPs present in cell media at different timepoints of a NP binding flow experiment. The concentration of ICAM-NP was calculated measuring the fluorescent intensity of the NP media and inserting the value into the linear regression equation from Figure 14. The media solutions are excited with a 488 nm laser and fluorescent intensity is recorded at 520 emission. The fluorescence of 5 samples are measured and stand deviation of the groups displayed.

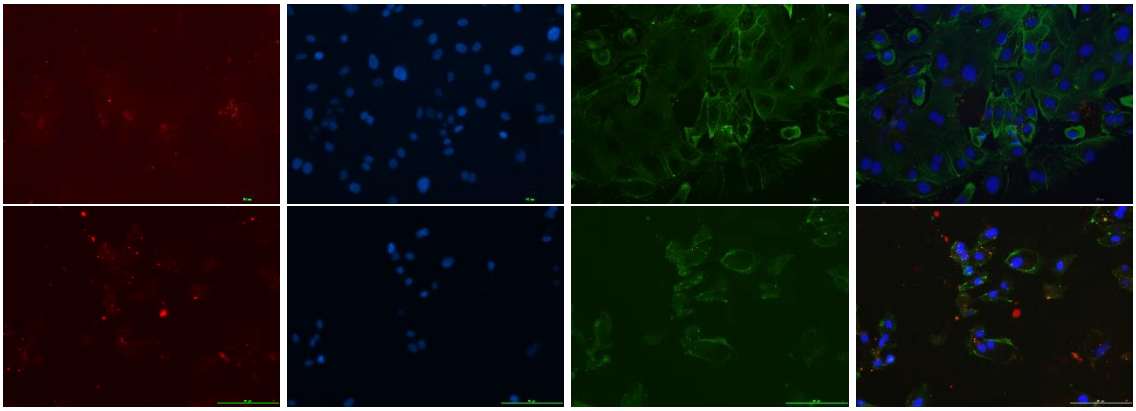

Figure 31. Fluorescent Images of NP Binding to Flow Adapted HUVECs.

Images from different fluorescent channels taken of microscope slide after 4 hours of ICAM NP binding. Images include Hoechst stains for the nuclei (blue), phalloidin 488 for the cell body (green), Alexa 568 for ICAM NPs (red), and the merged channel image. All samples are imaged at the same LED power and exposure to allow for comparison of fluorescent intensity. Scale bar measures 100 um.

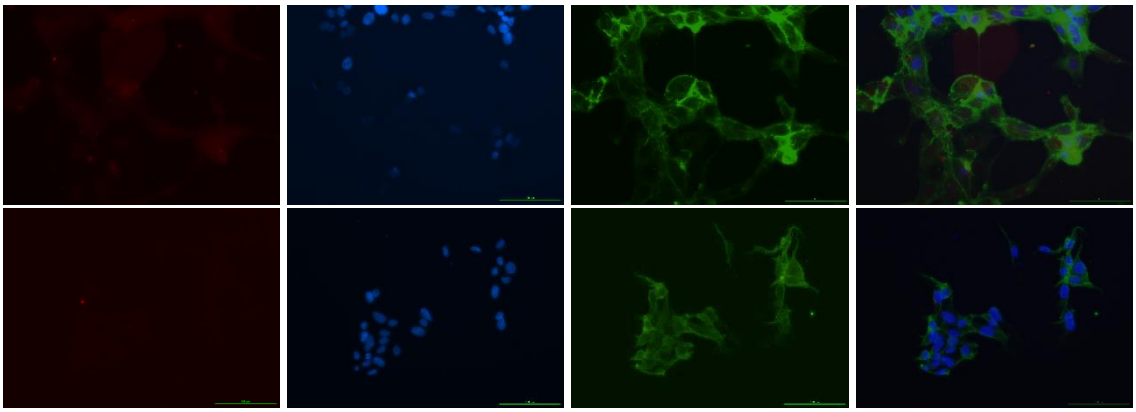

Figure 32. Fluorescent Images of Flow Adapted HUVECS without ICAM NPs.

Images from different fluorescent channels taken of microscope slide after 24 hours of TNF α activation. Images include Hoechst stains for the nuclei (blue), phalloidin 488 for the cell body (green), Alexa 568 (red), and the merged channel image. All samples are imaged at the same LED power and exposure to allow for comparison of fluorescent intensity. Scale bar measures 100 um.

Chapter IV.

Discussion

The results obtained from DLS experiments represents the mean particle size based on three types of distributions; intensity, volume, and number. As shown with an ANOVA one-way test, there is a statistically significant difference between the mean size obtained from each of these distributions (Table 1). To correctly analyze the DLS size results, it's important to understand how each of these distributions are formed, what each of these distributions represents.

DLS is a technique that measures the random movement of particles in solution (known as Brownian motion) and relates this motion to the size of the particles. To measure the Brownian motion of the particles, the DLS device will shine a beam of light through a particle solution, which results in the light being scattered, and measures the fluctuations in the scattered light intensity over a period of time. Since larger particles diffuse slower through a solution than smaller particles, the intensity fluctuations of the scattered light will determine how fast the particles diffuse and this can then be related to the size of the particle in the solution (Stetefeld, Mckenna & Patel, 2016).

The intensity distribution is the first order result from a DLS experiment and describes the amount of light scattered by particles in different size bins. The scattering intensity of light is proportional to r^6 (r is the radius of the particle in solution), which results in larger particles scattering much larger amounts of light than smaller particles (example: a 100 nm particle scatters $1x10^6$ more light than a 10 nm particle (Mansfield et al., 2017). This means that if there are any aggregates in the solution being measured, the intensity distribution will be skewed towards these particles. This phenomenon is clearly

present in our results, as the intensity distribution of each NP formation group is larger than both the number and volume distribution (Table 1). This makes the intensity distribution less accurate as a representation of the true size of the NPs.

The intensity distribution can be converted using Mie theory to a number and volume distribution (International Organization for Standardization, 2017). The volume distribution represents the total volume of particle in different size bins, while the number distribution shows the number of particles in different size bins. These results are more normalized than the intensity distribution results, however the volume distribution will still be towards larger particles due to the nature of the intensity. This phenomenon can be explained by comparing the number and volume distribution of a theoretical example of 100 particles, evenly distributed at 1 um, 2 um and 3 um (Figure 32). Although the particles represented in the graphs are the same, most of the total particle volume in the volume distribution is due to the 3 um particles (Figure 32B), even the though number of 3 um particles is the same as the 2 um and 1 um particle number (Figure 32A). This example helps to demonstrate why the mean particle size is large for all volume distributions comparted to the mean particle size obtained from the number distribution.

One way of determining which DLS distribution results are the most accurate representation of average particle size is by comparing these results to those obtained from SEM data. It's clear to see that the average size of the NP formation groups obtained from SEM image analysis is most closely related to the mean NP sizes obtained from the DLS number distribution results. The large difference in the SEM mean size compared to the volume and intensity distribution sizes is most likely a result of NP aggregates causing an increase in these two distribution results. The size ranges seen in

the DLS number distribution and SEM size analysis indicate a range from 120-150 nm, which is an ideal size range for NP drug delivery. While particles <~5nms display rapid renal clearance and particles >200 nm are filtered through the spleen, studies show that particles ~100 nm show the longest circulation time in vivo (Blanco, Shen & Ferrari, 2015).

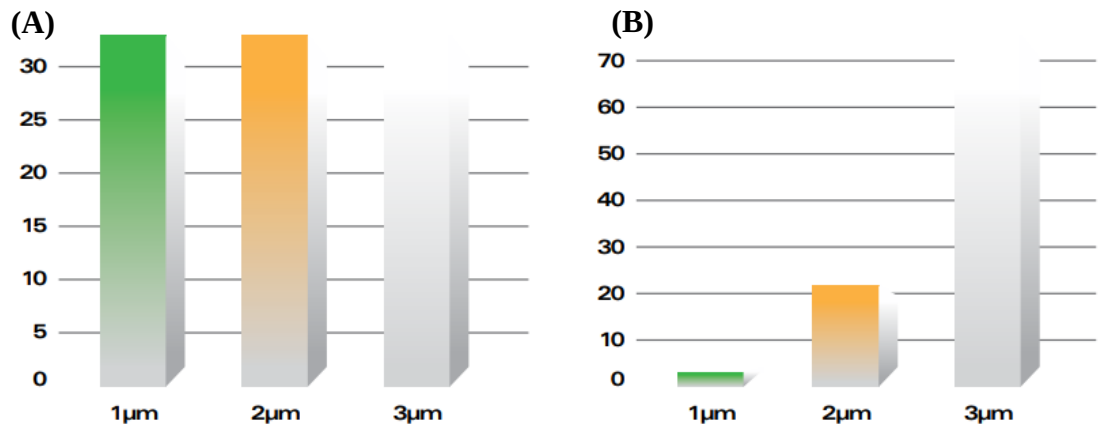

Figure 32. Comparison of Number and Volume Distribution.

Graph displaying (A) the number distribution and (B) the volume distribution of an example DLS data output. This visualization helps to show how the data from volume distribution can be misleading from the actual number distribution. Image from Horiba Scientific, 2018.

Zeta Potential Analysis

Zeta potential analysis is an essential characteristic for predicting the stability of NPs in solution, which can influence both binding and circulation of the NP (Nano Composix, 2012). Due to the inherent negative surface charge of NPs, in ionic solutions NPs will have an electrical double layer, consisting of ions both strongly bound to NP surface, and a layer of ions attracted to the NP surface but not bound (called the slipping

plane). As the NP moves through the solution, the ions that are attracted to it will move with it. The edge of the slipping plane refers to the maximum distance from the particle surface that oppositely charged ions will move with the NP (Griffiths et al., 2011). The zeta potential is the measure of the electrical potential at this electrical double layer. A higher level of zeta potential corresponds to a greater electrostatic repulsion between the NPs, which minimizes the changes of NP aggregation (Clogston & Patri, 2011).

In general, zeta potential values greater than or less than +25/-25 mV represent particles with high degrees of stability. The unmodified and unloaded PLGA-PEG molecule demonstrates a high level of stability, with a zeta potential of -27 +/- 1 mV. However, once the surface of the NP has been modified or drugs have been encapsulated, a significant increase in zeta potential can be seen. There are several factors that could cause the increase in zeta potential seen, each specific to the cargo or molecule added.

When the anti-ICAM antibody is modified to the surface of the nanoparticle, the zeta potential increases from -27 to -12.5 mV ($p<0.0001$). There could be multiple reasons for this change in zeta potential. The first could be that the attachment of the ICAM antibody to the surface of the NP reduces the amount of carboxylic functional groups available at the NP surface, which has been shown to reduce the zeta potential of the NP (Manoochehri et al., 2013). Another possible reason could be due to the isoelectrical point (*pI*) of the anti-ICAM antibody. The *pI* is defined as the pH at which a protein has no net charge; when the pH of a solution is greater than the antibody's *pI* the protein has a negative charge, and when the pH of a solution is less than the antibody's *pI* the protein has a positive charge (Schneider, 2017). The anti-ICAM antibody which has been modified to the surface of the NP is a mouse IgG2a antibody, and it has been shown

that this class of antibody can have *pI* values of 8 (Tron, Jacob & Bach, 1983). Since the zeta potential measurements are performed in diH20 at a pH of 7, the *pI* of the antibody could be contributing a positive charge that results in the overall decrease of the NP's zeta potential.

The encapsulation of both hypertensive drugs also resulted in a significant increase in zeta potential ($p<0.0001$). The effect of introducing a drug cargo during NP formation has previously been shown to alter the zeta potential of the NPs, and it has been hypothesized that this could be due to an unknown interaction of the drug with the NP (Gatti et al., 2018). Continuing with this theory, it is possible that the introduction of the drug during the NP formation process effects the placement of the PLGA-PEG copolymer in the NP structure. When PLGA-PEG copolymers are dissolved in an organic solution and added to an aqueous solution, the copolymer will spontaneously assemble to form the PEG molecule on the outer surface of the NP with the PLGA polymer towards the interior of the NP. It is possible that the interaction of the drugs with the PLGA-PEG copolymer alters the amount of PEG exposed to the surface of the NP, which would affect the surface charge and thus the zeta potential of the NP. Further studies can be performed to analyze the amount of PEG molecules on the surface of drug-encapsulated NPs compared to non-loaded NP's.

FTIR Spectrum Analysis

The presence of the PEG molecule is confirmed using FTIR spectroscopy techniques. Since chemical groups display specific vibrations when excited at a specific wavelength, a unique absorbance spectrum can be obtained when a sample is excited with a broad band light. To compare the absorbances of the PEG-PLGA and PLGA NPs, the

spectrums are subtracted from each other and the differences in the absorbances can be observed. Figure 9 shows large differences in the two samples spectrums, which already indicates a difference in their chemical composition. The peaks at 1760 and 1380 (indicated with blue arrows) are generated from the C=O and CH3 group in PLGA, and both peaks are present in both spectrums, which indicates the presence of the PLGA polymer in both samples (Xiao & Wang, 2015). This confirms that the samples tested contain the PLGA polymer used during NP synthesis, instead of the other chemicals used during the process.

To determine if the attachment of the PEG molecule is causing the differences seen in the two spectrums, we can compare the PEG molecule spectrum to that of the subtracted spectrum from Figure 9. By comparing these two spectrums, we can see peaks at 2860 cm^{-1} (indicated with blue arrows), that are due to -CH stretching, which has been shown to be a characteristic peak in PEG molecules in FTIR spectrums (Figure 10) (Chieng et al., 2014). We also see large peaks present at 1475 cm^{-1} and 1350 cm^{-1} (indicated with orange arrows) that are present in both the PEG only spectrum, and the subtracted spectrum. This is a clear indication that the absorbance peaks of the subtracted spectrum are due to the attachment of the PEG molecule to the PLGA polymer. Although the PEG peaks observed from 900 to 1100 have different characteristics than the subtracted spectrum peaks, this could be due to the changes in PEG vibrations once the molecule is attached to the PLGA. We also see large peaks in the subtracted from 1900 – 2300 cm^{-1} that are not present in the PEG only spectrum, and these peaks are most likely due to the unwashed EDC or NHS that was used during PLGA activation.

Another way to determine if the peaks seen in the subtracted spectrum are due to the attachment of the PEG molecule is by comparing the subtracted spectrum to the FTIR software's built in spectrum library (Figure 11). The spectrums with the three highest matches that the library presents are all forms of the PEG molecule. The first two spectrums are displayed and compared to the subtracted spectrum. The library PEG spectrums show high peaks around 1100 cm^{-1}(indicated with blue arrows) which is characteristic of C-O stretching and can be seen in both the PEG library spectrums, as well as a small peak of our own (Pereira et al., 2016).

Although we are able to conclude with reasonable certainty that the PEG molecule was successfully attached during the PLGA-PEG synthesis process, this technique has the dissonance of offering no way to quantify how many of the PEG molecules have attached during the process. The amount of PEG conjugated to the surface of the NP has been shown to directly correspond to microsomal cellular uptake and increased blood circulation (Xu et al., 2015). These aspects are critical for the NP, as the absorption across the mucosal surface provides the NP access to the blood stream, and increased blood circulation time ensures the NP can completely release the encapsulated drug. Future experiments can be performed to determine the amount of PEG molecule conjugated to the NP and ensure the PEG concentration is high enough for adequate drug delivery.

ICAM Antibody Attachment

The choice to modify the surface of the NP with ICAM antibodies was made based on knowledge that highly upregulated levels of ICAM receptors are found in hypertensive patients, and that the molecular target of one of the encapsulated drugs is

primarily located at the surface of these cell types (Howard et al., 2014, Blair, Haven & Bauer, 2016). To confirm the presence of the ICAM antibody on the surface of the NP, a colorimetric protein test is run, and the absorbance of the samples is compared to those of a protein calibration curve to obtain the amount of ICAM antibody added. The test offers positive results, giving us a concentration of 50 ug/ml for the PLGA-ICAM NPs (Table 3). However, we see that the unconjugated PLGA-PEG NPs also display a certain amount of absorbance giving us a false protein concentration (6 ug/ml). This must mean there is an innate reaction of the PLGA or PEG that causes a certain level of absorbance. If we subtract this value from the ICAM NP concentration, we have a new value of 44 ug/ml. This demonstrates that the ICAM antibody has been successfully conjugated to the surface of the NP.

To characterize the amount of ICAM antibody successfully conjugated to the NP, we can compare the concentration results of the plate reader test to the initial amount of ICAM added. The plate reader test was performed at a 1 mg/ml NP concentration, which means that 44 ug of ICAM is attached per mg of NP. However, the initial amount of ICAM added was at a concentration of 11.6 ug antibody per mg of NP, which is counterintuitive as the results of the assay show there is more ICAM antibody present then added to the initial formulation. A possible explanation of this result could be the selection of BSA as the standard for the test. Each protein will react differently to the protein reagent dye used for this experiment, and the amount of color generated will differ depending on the various properties of the antibody (amino acid sequence, isoelectric point, secondary structure…) (Thermo Fisher Scientific, 2018). It is possible that one or more of the features of the ICAM antibody causes it to react differently to the

protein reagent than the BSA protein does. This would make the comparison of the ICAM absorbance to the BSA absorbance an inaccurate way to measure the concentration of the ICAM antibody. To obtain a more accurate concentration of the ICAM antibody on the surface of the NP, future experiments could rerun this assay using a protein closer related to the ICAM antibody for the generation of a more accurate standard curve.

Alexa 488 Attachment

To visualize the NPs during cell experiments and detect the presence of the NPs in cell media, a fluorescent Alexa molecule is attached to the surface of the NPs. To confirm the attachment of the fluorescent molecule to the NP, a fluorescent plate reader assay is run, and the fluorescent intensity of Alexa conjugate NP and unconjugated NP is compared (Table 4). The Alexa attachment procedure was shown to be successfully, confirming the ability of the NP to be visualized both in fluorescent imaging, and in cell media. These results are further confirmed through the successful visualization of the NPs during fluorescent imaging (Figure 24).

The amount of Alexa conjugated at the surface of the NP can be calculated by comparing the Alexa 488 fluorescent standard curve (Figure 13) to the fluorescent intensity of a known Alexa NP concentration (Figure 14). The amount of Alexa 488 conjugated per mg of NP is calculated to be 0.021 ug. When compared to the original amount of Alexa added (0.4 ug Alexa per mg of NP), only 0.05% of the Alexa molecule has been successfully attached. This is an extremely low attachment percent, and while it was enough to successfully run the fluorescent experiments, a higher amount of attachment could help to generate more precise results. Future experimentation of the

concentration of NHS and EDC can be evaluated to identify an ideal concentration for increased Alexa attachment.

Drug Loading and Drug Release

The ability to successfully deliver a sustained release of encapsulated drug is dependent on the amount of drug successfully encapsulated in the NP. The encapsulation efficiency of the drugs varies greatly, with Captopril showing a much higher percent when compared to Valsartan (Table 5). This result is not surprising, as it's previously been shown that encapsulation efficiency is positively correlated with the lipophilicity of drugs, and Captopril is a highly lipophilic drug (Barichello et al., 1999). During the NP formulation process, as the organic phase is added to aqueous phase, Captopril is much more likely to remain the lipophilic organic phase rather than disperse into the aqueous phase, which would result in a higher amount of drug encapsulated into the NP. Although the encapsulation efficiency of Valsartan is much lower than that of Captopril, the entrapment of any amount of drug offers promising results. Further experiments to increase entrapment can test the organic solvent used, as well as the drug to polymer ratio.

Although the drug entrapment characteristics of the NPs is important to understand, the release rate of the drugs from the NP is far more essential for the purposes of this study. The sustained release of the drug from the PLGA NP is an attempt to reduces the amount of drug doses required per day, by replenishing the drug that the body has removed from the blood stream. Both Captopril and Valsartan showed a significantly sustained release profile where all 100% of the drug has been released by the 4^{th} day (Figure 19, Figure 20). These results are extremely promising, as the half-lives

of Captopril and Valsartan is 2 hours and 4 hours respectively (Duchin, Singhvi, Willard, Migdalof & Mckinstry, 1982, Flesch, Muller & Lloyd, 1997). The ability to provide the release of each drug over the course of multiple days would significantly reduce the number of doses required, which would help to improve the patient's adherence to the drug treatment regime.

Cell Binding Experiments

The ability of the ICAM-NP to bind to activated cells is an essential property of the NP, as the ICAM antibody allows the specific targeting of the NP. The binding ability of ICAM NPs is compared to those of Alexa NPs to determine the importance of the antibody on the NPs ability to bind to the cell (Figure 23). Although the Alexa NP is able to bind to the activated cells, the amount of NP binding significantly increases with the presence of the ICAM antibody. This increase in binding is essential, as the targeted drug delivery to the pulmonary endothelium has been shown to provide increased therapeutic results in comparison to non-targeted treatments (Gupta, 2014).

The timeline for ICAM-NP binding is important to ensure that the NP can bind to the target cells before they are cleared from the blood stream. The ICAM-NPs showed significant binding levels in just 30 mins, and the level of binding continued to increase over the 4-hour time period (Figure 26). This indicates the affinity of the ICAM-NP to the activated HUVECS and indicates that a significant number of NPs would be able to bind to the target cells before they are cleared from the blood stream. Just as important as understanding the ability of the ICAM-NPs to bind to activated HUVECs is understanding their ability to bind to unactivated cells. Since the target for the encapsulated drugs is located on the cell surface of the pulmonary vasculature, the drugs

would be less likely to reach their target if the NP was bound elsewhere in the body. Although the only way to confirm this trait would be through in vivo experimentation, an initial step to understanding the specificity of the ICAM-NP was performed by testing the binding of the ICAM NP to the unactivated cell line. Although the ICAM-NPs bound to the unactivated HUVECS, there was a significant increase in the amount of binding when the HUVECS were activated with TNF α (Figure 28). Even without the presence of TNF α, HUVECs display a level of ICAM receptor density, so a certain amount of binding is expected to these cells. Future experiments can be performed testing the ICAM NP binding over a variety of cell types, which would provide greater insight into the specificity of the ICAM NP binding.

The initial static experiments for ICAM NP binding were promising and proved the success in ICAM NP binding. However, these results offer only a partial understanding on the ability of the ICAM NP to bind, as these experiments were not done under physiologically relevant conditions. To further test the ICAM-NP binding abilities, a flow chamber was designed and machined to test HUVEC seeded microscope slides under physiologically relevant flow.

The initial results of the HUVEC binding to the glass slides were promising, as a confluent monolayer was formed during the experiment (Figure 29). However, after the slide was introduced into the flow chamber and adapted at adequate flow levels, a significant number of cells were lost, leaving only small clusters of cells around the edges of the slide. These results were found for both NP binding flow experiments, and control TNF α flow experiments, indicating the cause of the cell detachment was not influenced by the presence of NPs in the media. The detachment of the cells from the slide could be

the reason there were no significant changes seen in the ICAM-NP concentration in media; the cell density was so low that the number of nanoparticles bound to the surface did not significantly alter the NP concentration in the cell media during the course of the experiment (Figure 30).

There are multiple possibilities as to why the cells detached during flow; the first could be a problem with the coating on the glass slide, and the concentration of fibronectin was not high enough to keep the cells adhered under flow. Future experiments could be performed with different coating substances (such as gelatin or poly-l-lysine), which have both been used successfully for enhanced cell adhesion (Burns & Depaola, 2004). Another possibility could be due to the flow chamber assembly protocol and the formation of bubbles during the chamber assembly. The appearance of bubbles during flow experiments has been shown to cause significant cell detachment (Lane et al., 2012). These bubbles are formed when the chamber has not been adequately flushed prior to starting the flow experiments. Future experiments involving flow experiments would require extreme caution during the flow chamber set up to ensure all bubbles have been removed from the chamber and circuit prior to the start of the fluid flow.

Two types of analysis were used to test the amount of ICAM binding; fluorescent analysis of the cell medium both before and during the flow, as well as fluorescent imaging of the slide after the flow experiment. Unfortunately, due to the time constraints of the project, and the limited equipment availability, the microscopes that were accessible were unable to visualize the cells while they were held in the chamber. Having the ability to view the cells during the course of the experiment would have given insights onto the cause of cell detachment and allowed for adjustments to the protocol.

Despite these drawbacks, an initial understanding of the NP binding ability under flow can be obtained from the comparison of fluorescence of the NP binding slide (Figure 31) to that of the flow adapted cell slide (Figure 32). Although the overall cell number was significantly decrease, a small amount remained bound to the microscope slide and were able to be imaged for both experiments. The comparison of these two experiments shows the difference between the Alexa 568 fluorescent intensity, which corresponds to the secondary antibody for the ICAM NP. These results provide an initial demonstration of the ICAM-NPs ability to bind under flow, however further experiments would need to be performed before the binding ability of the NP can be confirmed.

Chapter V.

Bibliography

Alam, T., Khan, S., Gaba, B., Haider, F., Baboota, S., & Ali, J. (2017). Nanocarriers as treatment modalities for hypertension. *Drug Delivery, 24*(1), 358-369. doi:10.1080/10717544.2016.1255999

Alexander, M. R. (2017, March 23). Hypertension. Retrieved from https://emedicine.medscape.com/article/241381-overview#a2

Arora, A., Shafiq, N., Jain, S., Khuller, G. K., Sharma, S., & Malhotra, S. (2015). Development of Sustained Release 'NanoFDC (Fixed Dose Combination)' for Hypertension – An Experimental Study. *PLOS One, 10*(6). doi:10.1371/ journal.pone.0128208

Experiment studying a novel sustained release delivery system for hypertension drugs.Using PLGA nanoparticles, the researchers were able to demonstrate an increase in total drug release of up to 6 days.

AstraZeneca LP. (2012, October). PLENDIL® (felodipine) EXTENDED-RELEASE TABLETS. Retrieved from https://dailymed.nlm.nih.gov/dailymed/archives/fdaDrugInfo.cfm?archiveid=9336 8

Azizi, M., Linhart, A., Alexander, J., Goldberg, A., Menten, J., .., & Ménard, J. (2000). Pilot study of combined blockade of the renin–angiotensin system in essential hypertensive patients. *Journal of Hypertension, 18*(8), 1139-1147. doi:10.1097/00004872-200018080-00020

Barichello, J. M., Morishita, M., Takayama, K., & Nagai, T. (1999). Encapsulation of Hydrophilic and Lipophilic Drugs in PLGA Nanoparticles by the Nanoprecipitation Method. *Drug Development and Industrial Pharmacy, 25*(4), 471-476. doi:10.1081/ddc-100102197

Benjamin, E. J., Blaha, M. J., Chiuve, S. E., Cushman, M., Das, S., .., & Muntner, P. (2017). Heart Disease and Stroke Statistics—2017 Update: A Report From the American Heart Association. *Circulation, 135*. doi:10.1161/CIR.0000000000000485

Bhowmick, T., Berk, E., Cui, X., Muzykantov, V. R., & Muro, S. (2012). Effect of flow on endothelial endocytosis of nanocarriers targeted to ICAM-1. *Journal of Controlled Release, 157*(3), 485-492. doi:10.1016/j.jconrel.2011.09.067

Blair, L. A., Haven, A. K., & Bauer, N. N. (2016). Circulating microparticles in severe pulmonary arterial hypertension increase intercellular adhesion molecule-1 expression selectively in pulmonary artery endothelium. *Respiratory Research, 17*(1). doi:10.1186/s12931-016-0445-1

Blanco, E., Shen, H., & Ferrari, M. (2015). Principles of nanoparticle design for overcoming biological barriers to drug delivery. *Nature Biotechnology, 33*(9), 941-951. doi:10.1038/nbt.3330

Brown, M. T., & Bussells, J. K. (2011). Medication Adherence: WHO Cares? *SciVee*. doi:10.4016/27949.01

Burns, M. P., & Depaola, N. (2005). Flow-conditioned HUVECs support clustered leukocyte adhesion by coexpressing ICAM-1 and E-selectin. *American Journal of Physiology-Heart and Circulatory Physiology, 288*(1). doi:10.1152/ajpheart.01078.2003

Bélizaire, A., Tchistiakova, L., St-Pierre, Y., & Alakhov, V. (2003). Identification of a murine ICAM-1-specific peptide by subtractive phage library selection on cells. *Biochemical and Biophysical Research Communications, 309*(3), 625-630. doi:10.1016/j.bbrc.2003.08.050

Cagnoni, F., Njwe, C. A., Zaninelli, A., Ricci, A. R., Daffra, D., D'Ospina, A., . . . Destro, M. (2010). Blocking the RAAS at different levels: an update on the use of the direct renin inhibitors alone and in combination. *Vascular Health and Risk Management, 6*, 549-559. doi:10.2147/vhrm.s11816

Calderon, A. J., Muzykantov, V., Muro, S., & Eckmann, D. M. (2009). Flow dynamics, binding and detachment of spherical carriers targeted to ICAM-1 on endothelial cells. *Biorheology, 46*(4), 323-241. doi:10.3233/BIR-2009-0544

Canbakan, B. (2013). Rational approaches to the treatment of hypertension: drug therapy—monotherapy, combination, or fixed-dose combination? *Kidney International Supplements, 3*(4), 349-351. doi:10.1038/kisup.2013.75

Chamiot-Clerc, P., Copie, X., Renaud, J., Safar, M., & Girerd, X. (1998). Comparative reactivity and mechanical properties of human isolated internal mammary and radial arteries. *Cardiovascular Research, 37*(3), 811-819. doi:10.1016/s0008-6363(97)00267-8

Chieng, B. W., Azowa, I. N., Zin, W. Y., & Hussein, M. Z. (2014). Effects of Graphene Nanopletelets on Poly(Lactic Acid)/Poly(Ethylene Glycol) Polymer Nanocomposites. *Advanced Materials Research, 1024*, 136-139. doi:10.4028/www.scientific.net/amr.1024.136

Chittasupho, C., Xie, S., Baoum, A., Yakovleva, T., Siahaan, T. J., & Berkland, C. J. (2009). ICAM-1 targeting of doxorubicin-loaded PLGA nanoparticles to lung epithelial cells. *European Journal of Pharmaceutical Sciences, 37*(2), 141-150. doi:10.1016/j.ejps.2009.02.008

Chobanian, A., Bakris, G., & Black, H. (2003). The seventh report of the Joint National Committee on prevention, detection, evaluation, and treatment of high blood pressure. The JNC 7 report. *ACC Current Journal Review, 12*(4), 31-32. doi:10.1016/s1062-1458(03)00270-8

Clogston, J. D., & Patri, A. K. (2011). Zeta Potential Measurement, Characterization of Nanoparticles Intended for Drug Delivery. *Methods in Molecular Biology (Methods and Protocols), 697*. doi:https://doi-org.ezp-prod1.hul.harvard.edu/10.1007/978-1-60327-198-1_6

Conant, C. G., Schwartz, M. A., Nevill, T., & Ionescu-Zanetti, C. (2009). Platelet Adhesion and Aggregation Under Flow using Microfluidic Flow Cells. *Journal of Visualized Experiments,* (32). doi:10.3791/1644

Cutright, D. E., Beasley, J. D., & Perez, B. (1971). Histologic comparison of polylactic and polyglycolic acid sutures. *Oral Surgery, Oral Medicine, Oral Pathology, 32*(1), 165-173. doi:10.1016/0030-4220(71)90265-9

Dalpoas, S. E., & Samal, L. (2017, May 3). ACE inhibitors | Johns Hopkins Guides. Retrieved from https://www.hopkinsguides.com/hopkins/view/Johns_Hopkins_Diabetes_Guide/547002/all/ACE_inhibitors

Danhier, F., Ansorena, E., Silva, J. M., Coco, R., Breton, A. L., & Préat, V. (2012). PLGA-based nanoparticles: An overview of biomedical applications. *Journal of Controlled Release, 161*(2), 505-522. doi:10.1016/j.jconrel.2012.01.043

Excellent review of PLGA nanoparticles, detailing the number of advantages they offer, and focuses on understanding the specific characteristics that give PLGA NPs an advantage in drug delivery.

Detry, J. M., Block, P., De Backer, G., Degaute, J. P., & Six, R. (1995). Patient compliance and therapeutic coverage: comparison of amlodipine and slow release nifedipine in the treatment of hypertension. *European Journal of Clinical Pharmacology, 47*(6), 477-481. doi:10.1007/BF00193697

Dittrich, R., Parker, L., Rosen, J. B., Shangold, G., Creasy, G. W., & Fisher, A. C. (2002). Transdermal contraception: Evaluation of three transdermal norelgestromin/ethinyl estradiol doses in a randomized, multicenter, dose-response study. *American Journal of Obstetrics and Gynecology, 186*(1), 15-20. doi:10.1067/mob.2002.118844

Study conducted to compare cycle control and level of ovulation suppression of one weekly dosing versus daily dosing of contraceptives.Results showed that patients have a higher level of treatment compliance when required to administer treatment once a week versus once a day.

Duchin, K. L., Singhvi, S. M., Willard, D. A., Migdalof, B. H., & Mckinstry, D. N. (1982). Captopril kinetics. *Clinical Pharmacology and Therapeutics, 31*(4), 452-458. doi:10.1038/clpt.1982.59

Fakhari, A., Baoum, A., Siahaan, T. J., Le, K. B., & Berkland, C. (2011). Controlling Ligand Surface Density Optimizes Nanoparticle Binding to ICAM-1. *Journal of Pharmaceutical Sciences, 100*(3), 1045-1056. doi:10.1002/jps.22342

Ferrer, M. C., Shuvaev, V. V., Zern, B. J., Composto, R. J., Muzykantov, V. R., & Eckmann, D. M. (2014). ICAM-1 Targeted Nanogels Loaded with Dexamethasone Alleviate Pulmonary Inflammation. *PLoS ONE, 9*(7). doi:10.1371/journal.pone.0102329

Flesch, G., Müller, P., & Lloyd, P. (1997). Absolute bioavailability and pharmacokinetics of valsartan, an angiotensin II receptor antagonist, in man. *European Journal of Clinical Pharmacology, 52*(2), 115-120. doi:10.1007/s002280050259

Forouzanfar, M. H., Alexander, L., Anderson, R. H., Bachman, V. F., Biryukov, S., Brauer, M., . . . Wagner, J. (2015). Global, regional, and national comparative risk assessment of 79 behavioural, environmental and occupational, and metabolic risks or clusters of risks in 188 countries, 1990–2013: a systematic analysis for the Global Burden of Disease Study 2013. *The Lancet, 386*(10010), 2287-2323. doi:10.1016/S0140-6736(15)00128-2

- Annual update of the Global Burden of Disease; analyzes risk factors and emerging threats to the populations health such as hypertension, malnutrition, and tobacco smoke.• Variety of statistics about hypertension in US and worldwide.

Gatti, T. H., Eloy, J. O., Ferreira, L. M., Silva, I. C., Pavan, F. R., Gremião, M. P., & Chorilli, M. (2018). Insulin-loaded polymeric mucoadhesive nanoparticles: Development, characterization and cytotoxicity evaluation. *Brazilian Journal of Pharmaceutical Sciences, 54*(1). doi:10.1590/s2175-97902018000117314

Gonzalez-Rodriguez, D., & Barakat, A. I. (2015). Dynamics of Receptor-Mediated Nanoparticle Internalization into Endothelial Cells. *Plos One, 10*(4). doi:10.1371/journal.pone.0122097

Grabowski, E. F., & Mcdonnell, S. L. (1993). Human versus bovine endothelial cell culture on glass and tissue-culture plastic. *Journal of Tissue Culture Methods, 15*(4), 190-198. doi:10.1007/bf02388319

Griffiths, D., Brent, W., Hole, P., Smith, J., Malloy, A., & Carr, B. (2011). Zeta Potential Measurement of Nanoparticles by Nanoparticle Tracking Analysis (NTA). *Nano Science and Technology Institute (NSTI), 1*(2011). doi:ISBN 978 1-4398-7142-3

Gupta, N. (2014). Inhalable micelles expressing a lung-targeting peptide for delivery of therapies to treat pulmonary arterial hypertension (PAH). *Science-Business EXchange, 7*(43), 1276-1276. doi:10.1038/scibx.2014.1276

Hines, D. J., & Kaplan, D. L. (2013). Poly(lactic-co-glycolic) Acid-Controlled-Release Systems: Experimental and Modeling Insights. *Critical Reviews in Therapeutic Drug Carrier Systems, 30*(3), 257-276. doi:10.1615/critrevtherdrugcarriersyst.2013006475

Horiba Scientific. (2018). A Guidebook to Particle Size Analysis. Retrieved from https://www.horiba.com/fileadmin/uploads/Scientific/eMag/PSA/Guidebook

Houchin, M., & Topp, E. (2008). Chemical Degradation of Peptides and Proteins in PLGA: A Review of Reactions and Mechanisms. *Journal of Pharmaceutical Sciences, 97*(7), 2395-2404. doi:10.1002/jps.21176

Howard, M. D., Hood, E. D., Zern, B., Shuvaev, V. V., Grosser, T., & Muzykantov, V. R. (2014). Nanocarriers for vascular delivery of anti-inflammatory agents. *Annual Review of Pharmacology and Toxicology, 54*, 205-226. doi:10.1146/annurev-pharmtox-011613-140002

International Organisation for Standardisation. (2017-02). Methods for Determination of Particle Size Distribution Part 8: Photon Correlation Spectroscopy. *ISO 22412:*.

Izzo, J. L., & Weir, M. R. (2011). Angiotensin-Converting Enzyme Inhibitors. *The Journal of Clinical Hypertension, 13*(9), 667-675. doi:10.1111/j.1751-7176.2011.00508.x

Jain, R. A. (2000). The manufacturing techniques of various drug loaded biodegradable poly(lactide-co-glycolide) (PLGA) devices. *Biomaterials, 21*(23), 2475-2490. doi:10.1016/s0142-9612(00)00115-0

Jana, U., Mohanty, A. K., Pal, S. L., Manna, P. K., & Mohanta, G. P. (2014). Felodipine loaded PLGA nanoparticles: preparation, physicochemical characterization and in vivo toxicity study. *Nano Convergence, 1*(1). doi:10.1186/s40580-014-0031-5

Kumari, A., Yadav, S. K., & Yadav, S. C. (2010). Biodegradable polymeric nanoparticles based drug delivery systems. *Colloids and Surfaces B: Biointerfaces, 75*(1), 1-18. doi:https://doi.org/10.1016/j.colsurfb.2009.09.001

Lane, W. O., Jantzen, A. E., Carlon, T. A., Jamiolkowski, R. M., Grenet, J. E., Ley, M. M., . . . Achneck, H. E. (2012). Parallel-plate Flow Chamber and Continuous Flow Circuit to Evaluate Endothelial Progenitor Cells under Laminar Flow Shear Stress. *Journal of Visualized Experiments,* (59). doi:10.3791/3349

Manolis, A. J., Poulimenos, L. E., & Kallistratos, M. S. (2015). Arterial hypertension: benefits and limitations of treatment. *ESC Council for Cardiology Practice, 13*(28).

Manoochehri, S., Darvishi, B., Kamalinia, G., Amini, M., Fallah, M., Ostad, S. N., . . . Dinarvand, R. (17 july 2013). Surface modification of PLGA nanoparticles via human serum albumin conjugation for controlled delivery of docetaxel. *DARU Journal of Pharmaceutical Sciences, 21*(1), 58. doi:10.1186/2008-2231-21-58

Manrique, C., Lastra, G., Gardner, M., & Sowers, J. R. (2009). The renin angiotensin aldosterone system in hypertension: roles of insulin resistance and oxidative stress. *Medical Clinics of North America, 93*(3), 569-582. doi:10.1016/j.mcna.2009.02.014

Mansfield, E., Kaiser, D. L., Fujita, D., & Voorde, M. V. (2017). *Metrology and Standardization of Nanotechnology: Protocols and Industrial Innovations*. Wiley-VCH.

Mazzaglia, G., Ambrosioni, E., Alacqua, M., Filippi, A., Sessa, E., .., & Mantovani, L. (2009). Adherence to Antihypertensive Medications and Cardiovascular Morbidity Among Newly Diagnosed Hypertensive Patients. *Circulation, 120*, 1598-1605. doi:10.1161/CIRCULATIONAHA.108.830299

Meredith, P. A., Perloff, D., Mancia, G., & Pickering, T. (1995). Blood Pressure Variability and Its Implications for Antihypertensive Therapy. *Blood Pressure, 4*(1), 5-11. doi:10.3109/08037059509077561

Mohaimen, N. A., Sami, A., Al-assady, Z. T., & Ali, A. J. (2013). Intercellular adhesion molecules -1 (ICAM-1) and Vascular cell adhesion molecules-1 (VCAM-1) in hypertensive patients suffering from bacterial UTIs. *Kerbala Journal of Pharmaceutical Sciences Number, 5*.

Morelli, J., & Ogbru, O. (2016, April 25). High Blood Pressure (Hypertension) Medications; Peripheral Adrenergic Inhibitors.

Murciano, J. C., Muro, S., Christofidou-Solomidou, M., Harshaw, D. W., Albelda, S. M., Granger, D. N., . . . Muzykantov, V. R. (2003). ICAM-directed vascular immunotargeting of antithrombotic agents to the endothelial luminal surface. *Blood, 101*(10), 3977-3984. doi:10.1182/blood-2002-09-2853

Study testing whether ICAM-1 is a suitable target for pulmonary vascular lumen.The experiment concluded that ICAM-1 can serve as a target for drug delivery to endothelium, as well as sites of inflammation.

Muro, S., & Muzykantov, V. (2005). Targeting of Antioxidant and Anti-Thrombotic Drugs to Endothelial Cell Adhesion Molecules. *Current Pharmaceutical Design, 11*(18), 2383-2401. doi:10.2174/1381612054367274

Muro, S., Dziubla, T., Qiu, W., Leferovich, J., Cui, X., Berk, E., & Muzykantov, V. (2006). Endothelial Targeting of High-Affinity Multivalent Polymer Nanocarriers Directed to Intercellular Adhesion Molecule 1. *Journal of Pharmacology and Experimental Therapeutics, 317*(3), 1161-1169. doi:10.1124/jpet.105.098970

Mutschler, E., & Knauf, H. (1999). Current status of sustained release formulations in the treatment of hypertension. An overview. *Clinical Pharmacokinetics, 37*(1), 1-6.

Muzykantov, V. R. (2013). Targeted Drug Delivery to Endothelial Adhesion Molecules. *ISRN Vascular Medicine, 2013*(Article ID 916254), 1-27. doi:10.1155/2013/916254

Nano Composix. (2012, September). Zeta Potential Analysis of Nanoparticles. Retrieved from https://cdn.shopify.com/s/files/1/0257/8237/files/nanoComposix_Guidelines_for_Zeta_Potential_Analysis_of_Nanoparticles.pdf

Nwankwo, T., Yoon, S. S., Burt, V., & Gu, Q. (2013). Hypertension among adults in the US: National Health and Nutrition Examination Survey, 2011-2012. *NCHS Data Brief, 133*.

Orfanos, S. E., Langleben, D., Khoury, J., Schlesinger, R. D., Dragatakis, L., Roussos, C., . . . Catravas, J. D. (1999). Pulmonary Capillary Endothelium-Bound Angiotensin-Converting Enzyme Activity in Humans. *Circulation, 99*, 1593-1599. doi:10.1161/01.CIR.99.12.1593

Study that characterizes pulmonary endothelial ACE in vivo

Pandya, V. P., Patel, B. V., & Patel, P. (2012). Formulation, evaluation and optimization of sustained release matrix tablets of captopril. *Journal of Pharmacy and Bioallied Sciences, 4*(5), 77. doi:10.4103/0975-7406.94146

Paz, N. G., Walshe, T. E., Leach, L. L., Saint-Geniez, M., & Damore, P. A. (2012). Role of shear-stress-induced VEGF expression in endothelial cell survival. *Journal of Cell Science, 125*(4), 831-843. doi:10.1242/jcs.084301

Pereira, E. D., Cerruti, R., Fernandes, E., Peña, L., Saez, V., Pinto, J. C., . . . Júnior, F. G. (2016). Influence of PLGA and PLGA-PEG on the dissolution profile of oxaliplatin. *Polímeros, 26*(2), 137-143. doi:10.1590/0104-1428.2323

Perucca, E. (2009). Extended-Release Formulations of Antiepileptic Drugs: Rationale and Comparative Value. *Epilepsy Currents, 9*(6), 153-157. doi:10.1111/j.1535-7511.2009.01326.x

Prisant, L. M., & Elliott, W. J. (2003). Drug Delivery Systems for Treatment of Systemic Hypertension. *Clinical Pharmacokinetics, 42*(11), 931-940. doi:10.2165/00003088-200342110-00001

Ritter, J. M. (2011). Dual blockade of the renin-angiotensin system with angiotensin converting enzyme (ACE) inhibitors and angiotensin receptor blockers (ARBs). *British Journal of Clinical Pharmacology, 71*(3), 313-315. doi:10.1111/j.1365-2125.2011.03918.x

Rothlein, R., & Wegner, C. (1992). Role of intercellular adhesion molecule-1 in the inflammatory response. *Kidney International, 41*(3), 617-619. doi:10.1038/ki.1992.94

Sah, H., Thoma, L. A., Desu, H. R., Sah, E., & Wood, G. C. (2013). Concepts and practices used to develop functional PLGA-based nanoparticulate systems. *International Journal of Nanomedicine, 8*(1), 747-675. doi:10.2147/ijn.s40579

Discusses the advantages of functionalizing the surface of PLGA NPs, and reviews current examples of functional PLGA-based nanoparticle delivery systems.

Schneider, Z. (2017, June 28). Importance of isoelectric point (pI) of antibodies. Retrieved from https://www.antibodysociety.org/importance-isoelectric-point-pi-antibodies/

Shanghvi, D., Chary, B., & Tyebji, Z. (2003). *U.S. Patent No. US20030035836 A1*. Washington, DC: U.S. Patent and Trademark Office.

Patent for an "Oral controlled release pharmaceutical composition for once-a-day therapy for the treatment and prophylaxis of cardiac and circulatory diseases "

Sharma, S., Parmar, A., Kori, S., & Sandhir, R. (2016). PLGA-based nanoparticles: A new paradigm in biomedical applications [Abstract]. *TrAC Trends in Analytical Chemistry, 80,* 30-40. doi:10.1016/j.trac.2015.06.014

Singh, R., & Lillard, J. W., Jr. (2009). Nanoparticle-based targeted drug delivery. *Experimental and Molecular Pathology, 86*(3), 215-223. doi:doi.org/10.1016/j.yexmp.2008.12.004

Srivastava, A., Yadav, T., Sharma, S., Kumari, A., & Mishra, N. (2016). Polymers in Drug Delivery. *Journal of Biosciences and Medicines, 04*(01). doi:10.4236/jbm.2016.41009

Stergiou, G., Skeva, I., Baibas, N., Roussias, L., .., & Mountokalakis, T. (2000). Additive hypotensive effect of angiotensin converting enzyme inhibition and angiotensin receptor antagonism in essential hypertension. *Journal of Cardiovascular Pharmacology, 35*(6), 937-941. doi:10.1016/s0895-7061(00)00538-0

Stetefeld, J., Mckenna, S. A., & Patel, T. R. (2016). Dynamic light scattering: A practical guide and applications in biomedical sciences. *Biophysical Reviews, 8*(4), 409-427. doi:10.1007/s12551-016-0218-6

The Editors of Encyclopaedia Britannica (Ed.). (n.d.). Renin-angiotensin system. In *Encyclopaedia Britannica*. Encyclopaedia Britannica.

Thermo Fisher Scientific. (n.d.). Overview of Protein Assays Methods. Retrieved from https://www.thermofisher.com/us/en/home/life-science/protein-biology/protein-biology-learning-center/protein-biology-resource-library/pierce-protein-methods/overview-protein-assays.html

Tron, F., Jacob, L., & Bach, J. F. (1983). Murine monoclonal anti-DNA antibodies with an absolute specificity for DNA have a large amount of idiotypic diversity. *Proceedings of the National Academy of Sciences, 80*(19), 6024-6027. doi:10.1073/pnas.80.19.6024

Turnbull, F. (2003). Effects of different blood-pressure-lowering regimens on major cardiovascular events: results of prospectively-designed overviews of randomised trials. *The Lancet, 362*(9395), 1527-1535. doi:10.1016/s0140-6736(03)14739-3

Uhrich, K. E., Cannizzaro, S. M., Langer, R. S., & Shakesheff, K. M. (1999). Polymeric Systems for Controlled Drug Release. *Chemical Reviews, 99*(11), 3181-3198. doi:10.1021/cr940351u

Weir, M., & Dzau, V. J. (1999). The renin-angiotensin-aldosterone system: a specific target for hypertension management. *American Journal of Hypertension, 12*(S9), 205-213. doi:10.1016/s0895-7061(99)00103-x

World Health Organization (2003). (n.d.). *Adherence to Long-Term Therapies: Evidence for Action*. doi:ISBN 92 4 154599 2

Xiao, H., & Wang, L. (2015). Effects of X-shaped reduction-sensitive amphiphilic block copolymer on drug delivery. *International Journal of Nanomedicine, 2015*(19), 1st ser., 5309-5325. doi:10.2147/ijn.s85230

Xu, Q., Ensign, L. M., Boylan, N. J., Schön, A., Gong, X., Yang, J., . . . Hanes, J. (2015). Impact of Surface Polyethylene Glycol (PEG) Density on Biodegradable Nanoparticle Transport in Mucus ex Vivo and Distribution in Vivo. *ACS Nano, 9*(9), 9217-9227. doi:10.1021/acsnano.5b03876

Yu, T., Zhao, S., Li, Z., Wang, Y., Xu, B., ..., & Yang, J. (2016). Enhanced and Extended Anti-Hypertensive Effect of VP5 Nanoparticles. *International Journal of Molecular Sciences, 17*(12), 1977. doi:10.3390/ijms17121977

Yu, X., Trase, I., Ren, M., Duval, K., Guo, X., & Chen, Z. (2016). Design of Nanoparticle-Based Carriers for Targeted Drug Delivery. *Journal of Nanomaterials, 2016*(Article ID 1087250), 1-15. doi:10.1155/2016/1087250

Zhang, N., Chittasupho, C., Duangrat, C., Siahaan, T. J., & Berkland, C. (2008). PLGA Nanoparticle−Peptide Conjugate Effectively Targets Intercellular Cell-Adhesion Molecule-1. *Bioconjugate Chemistry, 19*(1), 145-152. doi:10.1021/bc700227z.